Supporting Information (SI)

Connection Position Induced Aggregation-Diminished or Aggregation-Enhanced Organic Room Temperature Electrophosphorescence

Jiaxin Lou[a#], Lulin Xu[a#], Wanting Ju[a], Dong Wang [a], Tianlin Cheng[a], Weiguo Zhu[b], Ning Su[a,*], Junqiao Ding[a,*]

[a]*School of Chemical Science and Technology, Yunnan University, Kunming 650500, Yunnan, China*

[b]*Jiangsu Engineering Laboratory of Light-Electricity-Heat Energy-Converting Materials and Applications, School of Materials Science and Engineering, and Changzhou University, Changzhou 213164, China*

Corresponding author:

E-mail: suning@ynu.edu.cn

E-mail: dingjunqiao@ynu.edu.cn

Lou and Xu have the same contributions to this paper.

1. Methods

All reagents and chemicals were purchased from commercial sources and used without further purification. ^{1}H and ^{13}C nuclear magnetic resonance (NMR) spectra were performed on a Bruker Avance NMR spectrometer. Electrospray Ionization Mass Spectroscopy (ESI-MS) was measured on Agilent 1100 HPLC instrument. Elemental analyses were recorded by a Bio-Rad elemental analysis system. Thermal gravimetric analysis (TGA) was recorded on STA449F3 under nitrogen atmosphere at a heating rate of 10 °C/min, respectively. Cyclic voltammetry (CV) was measured on a CHI760E electrochemical analyzer using ferrocene/ferrocenium (Fc/Fc^{+}) as the reference and n-Bu_4NClO_4 (0.1 M) as the supporting electrolyte. The HOMO and LUMO energy levels were calculated by the equation: $E_{HOMO\ (or\ LUMO)} = -[E_{onset,\ ox}$ (or $E_{onset,\ red}) +4.8V]$, where $E_{onset,\ ox}$ is the onset value of the first oxidation wave and $E_{onset,\ red}$ is the onset value of the first reduction wave. UV-Vis absorption spectra were measured with Shimadzu Corporation UV-3600i. The steady-state PL spectra, room-temperature phosphorescent spectra were measured on a HORIBA FLUOROMAX_PLUS_P spectrofluorometer equipped with an integrating sphere and a liquid nitrogen-cooled optical cryostat (Vcrto®V-100) with an Cryocon 22C temperature controller. Time-resolved emission spectra (TRES) were measured on a Omni-λ3028i fluorescence lifetime system equipped with a AO-S-355-40mW source. The transient PL spectra were recorded in vacuum using Edinburgh fluorescence spectrometer (FLS-1000). The PL quantum yields (Φ_{PL}s) were measured on Hamamatsu Photonics K. K.

2. Theoretical simulations

Density functional theory (DFT) and time-dependent DFT (TDDFT) calculations were performed using the Gaussian 09 program packages to calculate the frontier molecular orbital distributions, and energies of the key transitions. First, the geometries in the ground state were directly obtained from the 3D structure of D31 and D32. Second, the excited states (S_1 and T_n below S_1) energies, spin-orbit coupling matrix elements of S_1-to-T_n and T_1-to-S_0 were calculated using TD-DFT at a B3LYP/6-31G(d) level

according to 3D structure. Third, hole and electron analysis were performed using Multiwfn program and visualized by VMD software.

3. Device fabrication and measurements

The ITO substrates with a sheet resistance of 15 Ω per square were cleaned by sequential ultra-sonication in detergent, deionized water, acetone, ethanol, and then exposed to UV-Ozone for 15 min. After being transferred into a vacuum chamber, all material layers as shown in Fig. 6a were deposited by vacuum evaporation in a vacuum chamber with a base pressure of $<3 \times 10^{-5}$ Pa. As for doped devices, mCP is doped into D31 or D32 at a varying doping concentration. Moreover, the sensitized devices of D32:S-Cz-BN (2.5 wt%) were also fabricated with the device structure of ITO/HATCN (3 nm)/TAPC (30 nm)/TCTA (5 nm)/mCP (5 nm)/EML/DPEPO (5 nm)/TmPyPB (40 nm)/Liq (1 nm)/Al (150 nm), in which the EML is composed with D32 and S-Cz-BN (2.5 wt%). Similar to the fabrication processes of doped and non-doped devices based on D31 and D32, HATCN, TAPC, TCTA, mCP, S-Cz-BN (2.5 wt%) doped in D32, DPEPO, TmPyPB, Liq and Al was evaporated on the ITO substrate, respectively. The current density-voltage characteristics were performed using an HP4140B picometer. And the luminance and electroluminescence (EL) spectra were recorded by Minolta LS-110 Luminance meter and Ocean Optics USB-4000 spectrometer, respectively. EQE was calculated from the EL spectrum, luminance and current density assuming a Lambertian emission distribution. All the measurements were carried out at room-temperature under ambient conditions without device encapsulation.

4. Experimental section

4.1 Synthesis of D31

DMAC-OH [1] (0.80 g, 2.65 mmol), Cs_2CO_3 (1.13 g, 3.46 mmol), 3 mL dry NMP and 3 mL dry toluene were added into a 50 mL three-necked round-bottom flask, and then the suspension was heated to 140℃ for 2 h under argon atmosphere. Afterwards, 3-fluorobenzophenone (0.46 g, 2.31 mmol) dissolved in 3 mL dry NMP was added to the

system. The mixture was heated to 160℃ and refluxed for overnight. After cooling to room temperature, the system was extracted with dichloromethane (100 mL), washed with distilled water (150 mL), dried with anhydrous magnesium sulfate, filtered and distilled to obtain the crude product. Subsequently, the crude product was further purified by silica gel column chromatography using petroleum ether/dichloromethane (v/v = 6:1) as the eluent to afford D31 as a white powder (0.50 g, 45%). ^{1}H NMR (600 MHz, DMSO) δ 7.70 (dd, *J* = 13.8, 7.3 Hz, 4H), 7.67 - 7.63 (m, 1H), 7.59 - 7.55 (m, 1H), 7.53 - 7.49 (m, 3H), 7.47 (d, *J* = 7.8 Hz, 1H), 7.38 (d, *J* = 7.3 Hz, 3H), 7.31 (s, 1H), 7.24 (d, *J* = 8.1 Hz, 1H), 7.19 (s, 1H), 6.99 - 6.95 (m, 1H), 6.92 - 6.88 (m, 1H), 6.79 (dd, *J* = 8.9, 2.7 Hz, 1H), 6.16 (dd, *J* = 22.3, 8.5 Hz, 2H), 1.60 (s, 6H). ^{13}C NMR (151 MHz, DMSO) δ 195.57 (s), 158.86 (s), 149.21 (s), 141.01 (s), 140.74 (s), 138.99 (s), 137.99 (s), 137.25 (s), 133.25 (s), 131.93 (s), 131.69 (s), 131.39 (s), 130.68 (s), 130.05 (s), 129.27 (s), 129.03 (s), 127.03 (s), 125.86 (s), 124.10 (s), 121.49 (s), 121.06 (s), 118.86 (s), 118.05 (s), 117.27 (s), 115.32 (s), 113.99 (s), 40.42 (s), 40.21 (s), 40.28 (s), 40.14 (s), 40.00 (s), 39.86 (s), 39.58 (s), 39.72 (s), 39.58 (s), 36.33 (s), 31.44 (s). ESI (m/z): calcd for $C_{34}H_{27}NO_2$ $[M+H]^+$482.2120, found 482.2117.

4.2 Synthesis of D32

The synthesis of D32 was similar to D31with a good yield of 80%. ^{1}H NMR (600 MHz, DMSO) δ 7.75 (d, *J* = 8.4 Hz, 2H), 7.72 - 7.68 (m, 4H), 7.66 - 7.62 (m, 1H), 7.60 - 7.56 (m, 1H), 7.56 - 7.52 (m, 2H), 7.48 (d, *J* = 7.7 Hz, 1H), 7.40 (d, *J* = 7.7 Hz, 2H), 7.33 (d, *J* = 2.7 Hz, 1H), 7.02 (d, *J* = 8.4 Hz, 2H), 7.00 - 6.96 (m, 1H), 6.93 - 6.89 (m, 1H), 6.83 (dd, *J* = 8.9, 2.7 Hz, 1H), 6.22 (d, *J* = 8.9 Hz, 1H), 6.16 (d, *J* = 8.2 Hz, 1H), 1.62 (s, 6H). ^{13}C NMR (151 MHz, DMSO) δ 194.87 (s), 162.70 (s), 148.50 (s), 140.97 (s), 140.73 (s), 138.36 (s), 137.96 (s), 132.79 (s), 132.03 (s), 131.72 (s), 131.39 (s), 131.12 (s), 129.82 (s), 129.32 (s), 129.10 (s), 128.96 (s), 127.06 (s), 125.86 (s), 121.13 (s), 119.34 (s), 118.49 (s), 116.37 (s), 115.35 (s), 114.02 (s), 40.41 (s), 40.28 (s), 40.14 (s), 40.00 (s), 39.86 (s), 39.72 (m), 39.58 (s), 36.37 (s), 31.42 (s). ESI (m/z): calcd for $C_{34}H_{27}NO_2$ $[M+H]^+$482.2120, found 482.2118.

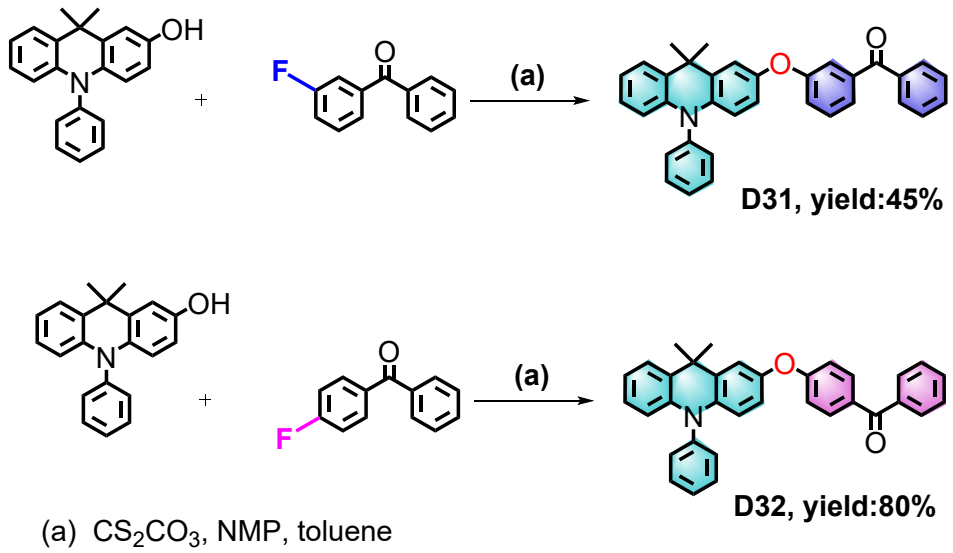

Scheme 1. The synthesis of D31 and D32.

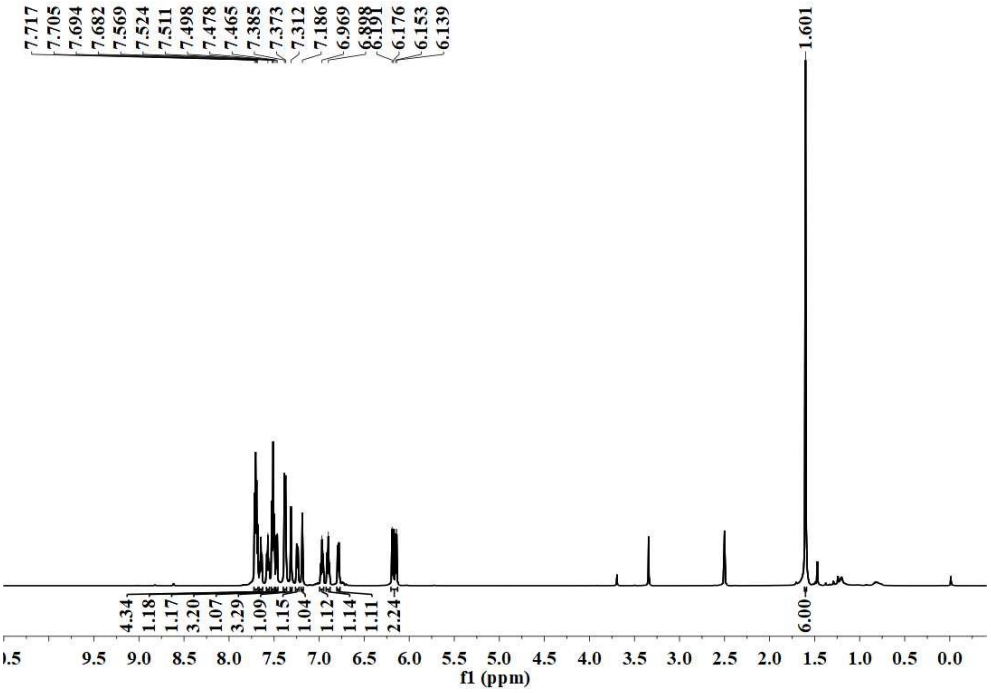

Fig. S1. ^{1}H NMR of D31.

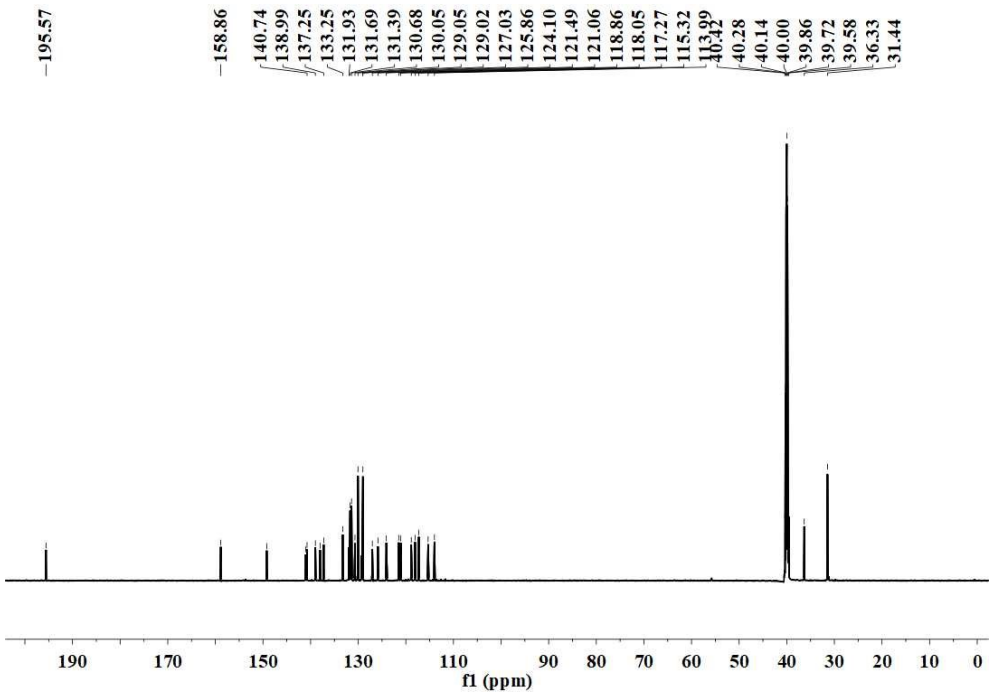

Fig. S2. ^{13}C NMR of D31.

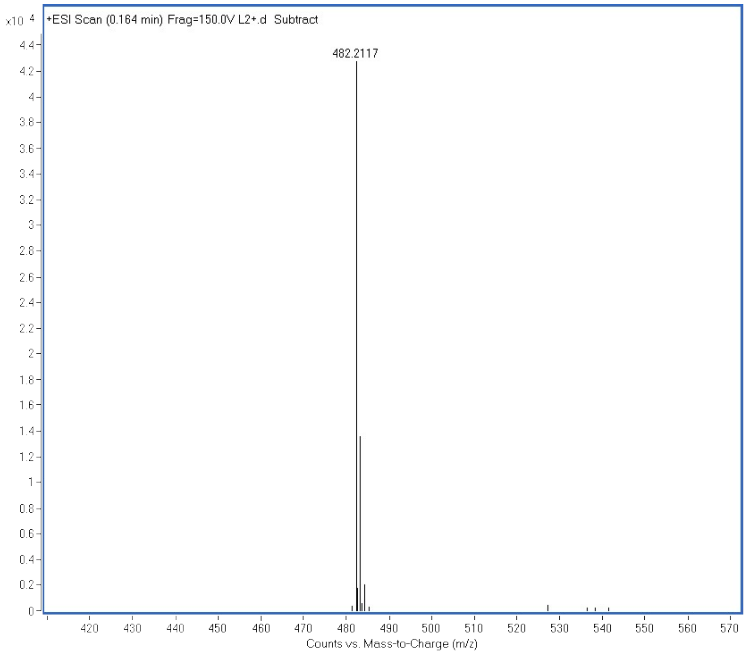

Fig. S3. Mass spectrum of D31.

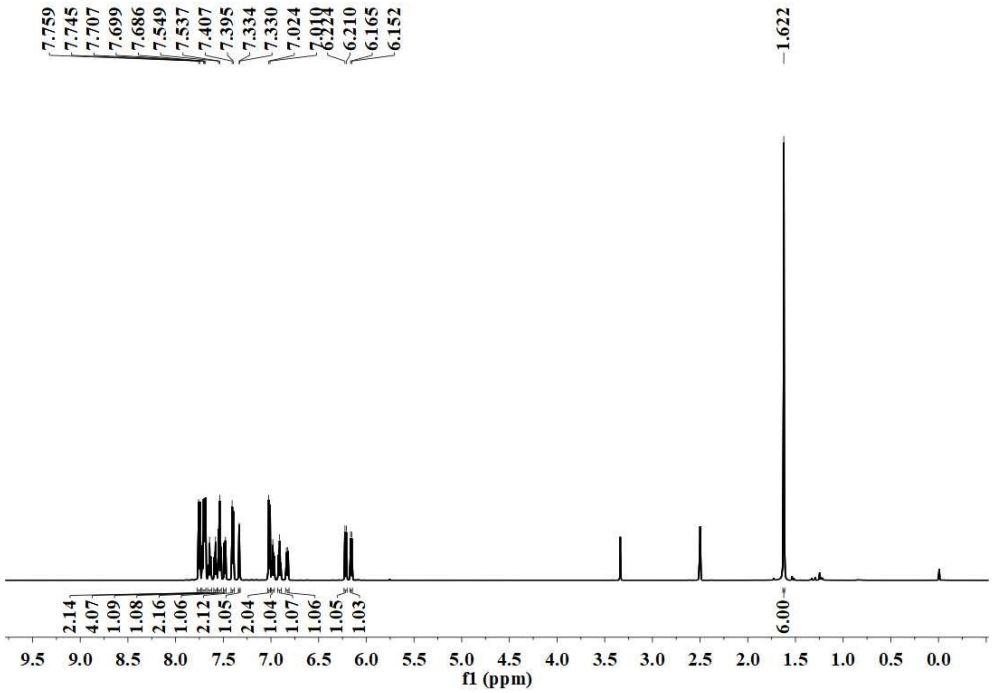

Fig. S4. ^{1}H NMR of D32.

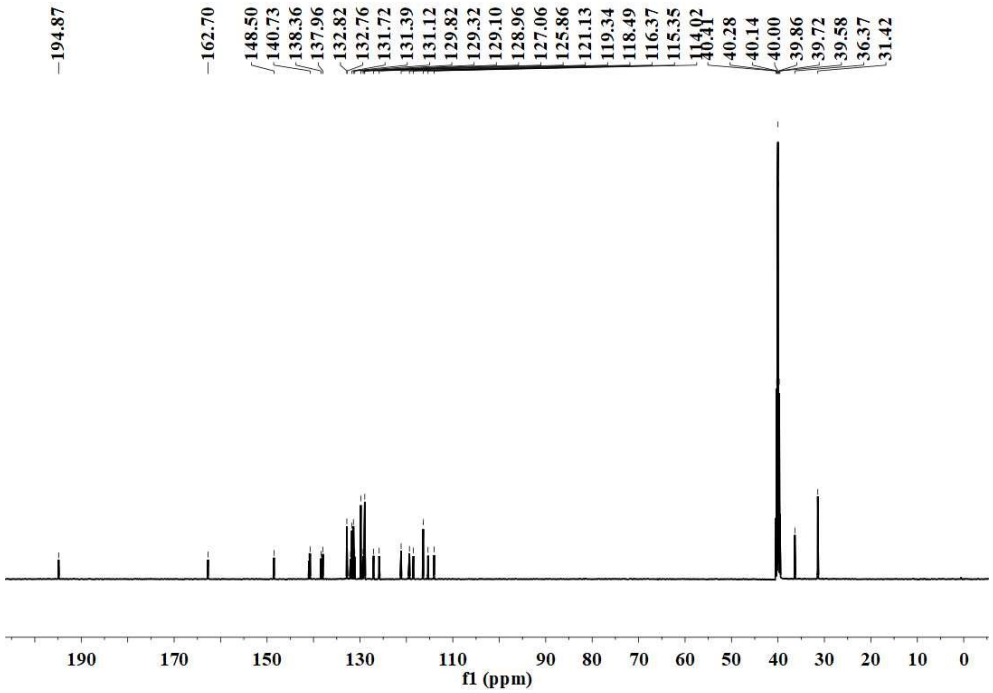

Fig. S5. ^{13}C NMR of D32.

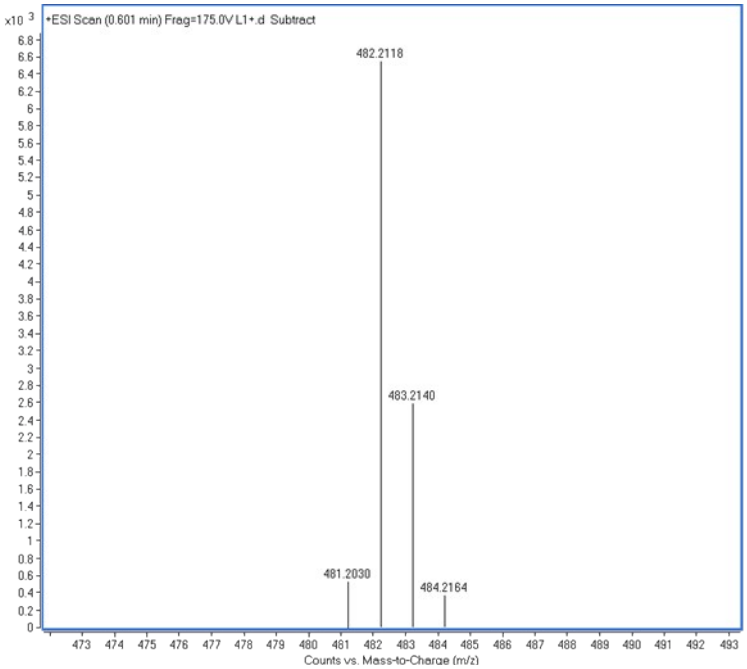

Fig. S6. Mass spectrum of D32.

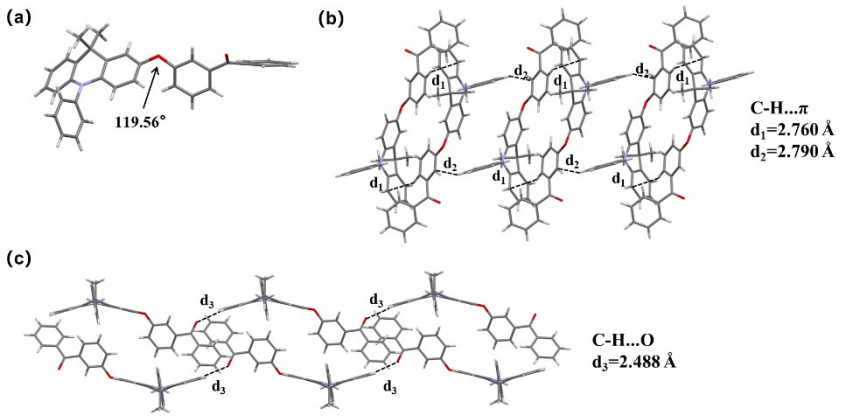

Fig. S7. (a) Single crystal structure and (b) packing pattern as well as intermolecular interactions of D31 (CCDC no. 2327606).

Table S1. X-Crystal data and structure refinement for D31 and D32.

	D31	D32
Empirical formula	$C_{34}H_{27}NO_2$	$C_{34}H_{27}NO_2$
Formula weight	481.56	481.56
Temperature/K	100 K	150 K
Crystal system	Triclinic	Monoclinic
Space group	P-1	P21/n

a/Å	8.1013(7)	10.7009(7)
b/Å	10.7557(11)	20.1981(15)
c/Å	14.6429(15)	11.7864(9)
α/°	92.302(5)°	90
β/°	93.992(4)°	94.071(3)°
γ/°	92.948(4)°	90
Volume/Å^3	1269.9(2)	2541.1(3)
Z	2	4
P_{calc} g/cm^3	1.259	1.259
Absorption coefficient/mm	0.078	0.078
F(000)	508	1016
Crystal size/mm^3	0.160 x 0.200 x 0.260	0.280 x 0.310 x 0.400
Radiation	MoKα (0.71073 Å)	MoKα (0.71073 Å)
Theta range for data collection/°	2.31 to 28.37	2.00 to 28.38
Index ranges	-10<=h<=10, -14<=k<=14, -19<=l<=19	-14<=h<=13, -26<=k<=26, -15<=l<=15
Reflections collected	41014	42199
Independent reflections	6344 [R(int) = 0.1002]	6343 [R(int) = 0.0525]
Data/restraints/parameters	6344 / 0 / 336	6343 / 0 / 336
Goodness-of-fit on F^2	1.041	1.034
Final R indexes [I>=2σ (I)]	R1 = 0.0494, wR2 = 0.1137	R1 = 0.0437, wR2 = 0.1032
Final R indexes [all data]	R1 = 0.0886, wR2 = 0.1366	R1 = 0.0713, wR2 = 0.1267
Largest diff. peak/hole / e Å^{-3}	0.245 and -0.251	0.220 and -0.220

Table S2. The bond length of D31.

D31	bond length (Å)	D31	bond length (Å)
O1-C20	1.396(2)	O1-C22	1.3773(19)
O2-C28	1.219(2)	N1-C1	1.4153(19)
N1-C11	1.410(2)	N1-C12	1.436(2)
C1-C2	1.397(2)	C1-C6	1.404(2)
C2-H2	0.95	C2-C3	1.389(2)

C3-H3	0.95	C3-C4	1.386(2)
C4-H4	0.95	C4-C5	1.388(2)
C5-H5	0.95	C5-C6	1.395(2)
C6-C7	1.520(2)	C7-C8	1.524(2)
C7-C9	1.550(2)	C7-C10	1.523(2)
C8-H8A	0.98	C8-H8B	0.98
C8-H8C	0.98	C9-H9A	0.98
C9-H9B	0.98	C9-H9C	0.98
C10-C11	1.405(2)	C10-C21	1.389(2)
C11-C18	1.398(2)	C12-C13	1.394(2)
C12-C17	1.382(2)	C13-H13	0.95
C13-C14	1.390(2)	C14-H14	0.95
C14-C15	1.382(3)	C15-H15	0.95
C15-C16	1.387(2)	C16-H16	0.95
C16-C17	1.389(2)	C17-H17	0.95
C18-H18	0.95	C18-C19	1.385(2)
C19-H19	0.95	C19-C20	1.382(2)
C20-C21	1.380(2)	C21-H21	0.95
C22-C23	1.385(2)	C22-C27	1.388(2)
C23-H23	0.95	C23-C24	1.389(2)
C24-C25	1.392(2)	C24-C28	1.499(2)
C25-H25	0.95	C25-C26	1.389(2)
C26-H26	0.95	C26-C27	1.388(2)
C27-H27	0.95	C28-C29	1.486(2)
C29-C30	1.391(3)	C29-C34	1.399(3)
C30-H30	0.95	C30-C31	1.387(3)
C31-H31	0.95	C31-C32	1.394(3)
C32-H32	0.95	C32-C33	1.380(3)
C33-H33	0.95	C33-C34	1.372(3)

C34-H34	0.95

Table S3. The bond angle of D31.

D31	bond angle (°)	D31	bond angle (°)
C22-O1-C20	119.57(12)	C1-N1-C12	117.70(13)
C11-N1-C1	118.90(13)	C11-N1-C12	119.71(12)
C2-C1-N1	121.31(14)	C2-C1-C6	119.92(14)
C6-C1-N1	118.75(14)	C1-C2-H2	119.8
C3-C2-C1	120.47(15)	C3-C2-H2	119.8
C2-C3-H3	120.0	C4-C3-C2	120.03(15)
C4-C3-H3	120.0	C3-C4-H4	120.3
C3-C4-C5	119.41(15)	C5-C4-H4	120.3
C4-C5-H5	119.1	C4-C5-C6	121.73(15)
C6-C5-H5	119.1	C1-C6-C7	118.03(13)
C5-C6-C1	118.24(14)	C5-C6-C7	123.51(14)
C6-C7-C8	112.80(13)	C6-C7-C9	107.39(13)
C6-C7-C10	108.06(12)	C8-C7-C9	108.41(13)
C10-C7-C8	112.83(13)	C10-C7-C9	107.05(12)
C7-C8-H8A	109.5	C7-C8-H8B	109.5
C7-C8-H8C	109.5	H8A-C8-H8B	109.5
H8A-C8-H8C	109.5	H8B-C8-H8C	109.5
C7-C9-H9A	109.5	C7-C9-H9B	109.5
C7-C9-H9C	109.5	H9A-C9-H9B	109.5
H9A-C9-H9C	109.5	H9B-C9-H9C	109.5
C11-C10-C7	118.17(14)	C21-C10-C7	123.14(14)
C21-C10-C11	118.43(14)	C10-C11-N1	118.80(13)
C18-C11-N1	121.54(14)	C18-C11-C10	119.64(14)
C13-C12-N1	120.91(14)	C17-C12-N1	118.96(14)
C17-C12-C13	120.09(15)	C12-C13-H13	120.2
C14-C13-C12	119.57(16)	C14-C13-H13	120.2

C13-C14-H14	119.9	C15-C14-C13	120.18(16)
C15-C14-H14	119.9	C14-C15-H15	119.9
C14-C15-C16	120.23(16)	C16-C15-H15	119.9
C15-C16-H16	120.1	C15-C16-C17	119.76(16)
C17-C16-H16	120.1	C12-C17-C16	120.17(15)
C12-C17-H17	119.9	C16-C17-H17	119.9
C11-C18-H18	119.6	C19-C18-C11	120.85(15)
C19-C18-H18	119.6	C18-C19-H19	120.5
C20-C19-C18	119.04(14)	C20-C19-H19	120.5
C19-C20-O1	122.00(14)	C21-C20-O1	117.01(14)
C21-C20-C19	120.71(15)	C10-C21-H21	119.4
C20-C21-C10	121.13(15)	C20-C21-H21	119.4
O1-C22-C23	115.22(14)	O1-C22-C27	124.09(15)
C23-C22-C27	120.66(15)	C22-C23-H23	120.2
C22-C23-C24	119.69(15)	C24-C23-H23	120.2
C23-C24-C25	120.23(15)	C23-C24-C28	117.46(14)
C25-C24-C28	122.08(15)	C24-C25-H25	120.3
C26-C25-C24	119.44(15)	C26-C25-H25	120.3
C25-C26-H26	119.7	C27-C26-C25	120.64(15)
C27-C26-H26	119.7	C22-C27-C26	119.33(15)
C22-C27-H27	120.3	C26-C27-H27	120.3
O2-C28-C24	119.50(16)	O2-C28-C29	120.47(16)
C29-C28-C24	120.02(15)	C30-C29-C28	121.25(16)
C30-C29-C34	119.69(18)	C34-C29-C28	118.85(17)
C29-C30-H30	120.0	C31-C30-C29	119.99(19)
C31-C30-H30	120.0	C30-C31-H31	120.2
C30-C31-C32	119.5(2)	C32-C31-H31	120.2
C31-C32-H32	119.8	C33-C32-C31	120.4(2)
C33-C32-H32	119.8	C32-C33-H33	119.9

C34-C33-C32	120.3(2)	C34-C33-H33	119.9
C33-C34-H34	119.9		

Table S4. The bond length of D32.

D32	bond length (Å)	D32	bond length (Å)
O2-C14	1.4046(17)	O2-C11	1.3681(17)
O1-C7	1.2248(17)	N1-C29	1.4386(17)
N1-C17	1.4052(18)	N1-C24	1.4089(18)
C32-H32	0.95	C32-C33	1.383(3)
C32-C31	1.389(3)	C33-H33	0.95
C33-C34	1.384(2)	C34-H34	0.95
C34-C29	1.387(2)	C29-C30	1.386(2)
C17-C16	1.3978(19)	C17-C18	1.4056(19)
C16-H16	0.95	C16-C15	1.385(2)
C15-H15	0.95	C15-C14	1.380(2)
C14-C19	1.379(2)	C11-C10	1.395(2)
C11-C12	1.390(2)	C10-H10	0.95
C10-C9	1.377(2)	C9-H9	0.95
C9-C8	1.395(2)	C8-C7	1.482(2)
C8-C13	1.4032(19)	C7-C1	1.495(2)
C1-C2	1.390(2)	C1-C6	1.390(2)
C2-H2	0.95	C2-C3	1.392(3)
C3-H3	0.95	C3-C4	1.376(3)
C4-H4	0.95	C4-C5	1.380(3)
C18-C19	1.393(2)	C18-C20	1.5210(19)
C19-H19	0.95	C6-H6	0.95
C6-C5	1.378(3)	C5-H5	0.95
C13-H13	0.95	C13-C12	1.379(2)
C12-H12	0.95	C20-C22	1.532(2)
C20-C23	1.524(2)	C20-C21	1.550(2)

C22-H22A	0.98	C22-H22B	0.98
C22-H22C	0.98	C23-C24	1.4080(19)
C23-C28	1.389(2)	C24-C25	1.399(2)
C25-H25	0.95	C25-C26	1.387(2)
C26-H26	0.95	C26-C27	1.382(2)
C27-H27	0.95	C27-C28	1.386(2)
C28-H28	0.95	C21-H21A	0.98
C21-H21B	0.98	C21-H21C	0.98
C30-H30	0.95	C30-C31	1.383(2)
C31-H31	0.95		

Table S4. The bond angle of D32.

D32	bond angle (°)	D32	bond angle (°)
C11-O2-C14	117.61(11)	C17-N1-C29	118.23(11)
C17-N1-C24	119.66(11)	C24-N1-C29	119.45(11)
C33-C32-H32	120.0	C33-C32-C31	119.97(15)
C31-C32-H32	120.0	C32-C33-H33	119.9
C32-C33-C34	120.20(16)	C34-C33-H33	119.9
C33-C34-H34	120.2	C33-C34-C29	119.66(15)
C29-C34-H34	120.2	C34-C29-N1	118.74(13)
C30-C29-N1	120.88(13)	C30-C29-C34	120.37(14)
N1-C17-C18	119.35(12)	C16-C17-N1	120.75(12)
C16-C17-C18	119.90(13)	C17-C16-H16	119.6
C15-C16-C17	120.81(13)	C15-C16-H16	119.6
C16-C15-H15	120.6	C14-C15-C16	118.72(13)
C14-C15-H15	120.6	C15-C14-O2	119.93(13)
C19-C14-O2	118.50(13)	C19-C14-C15	121.52(13)
O2-C11-C10	123.86(13)	O2-C11-C12	115.55(12)
C12-C11-C10	120.59(13)	C11-C10-H10	120.4

C9-C10-C11	119.23(13)	C9-C10-H10	120.4
C10-C9-H9	119.3	C10-C9-C8	121.34(13)
C8-C9-H9	119.3	C9-C8-C7	118.72(13)
C9-C8-C13	118.37(13)	C13-C8-C7	122.73(13)
O1-C7-C8	120.52(14)	O1-C7-C1	119.51(14)
C8-C7-C1	119.94(12)	C2-C1-C7	122.28(14)
C2-C1-C6	119.52(15)	C6-C1-C7	118.18(14)
C1-C2-H2	120.2	C1-C2-C3	119.63(17)
C3-C2-H2	120.2	C2-C3-H3	120.0
C4-C3-C2	120.05(18)	C4-C3-H3	120.0
C3-C4-H4	119.8	C3-C4-C5	120.43(17)
C5-C4-H4	119.8	C17-C18-C20	119.29(12)
C19-C18-C17	118.50(13)	C19-C18-C20	121.95(12)
C14-C19-C18	120.50(13)	C14-C19-H19	119.8
C18-C19-H19	119.8	C1-C6-H6	119.8
C5-C6-C1	120.38(17)	C5-C6-H6	119.8
C4-C5-H5	120.0	C6-C5-C4	119.91(19)
C6-C5-H5	120.0	C8-C13-H13	119.5
C12-C13-C8	120.94(13)	C12-C13-H13	119.5
C11-C12-H12	120.2	C13-C12-C11	119.51(13)
C13-C12-H12	120.2	C18-C20-C22	111.67(12)
C18-C20-C23	109.06(11)	C18-C20-C21	107.16(12)
C22-C20-C21	108.46(12)	C23-C20-C22	112.50(12)
C23-C20-C21	107.78(12)	C20-C22-H22A	109.5
C20-C22-H22B	109.5	C20-C22-H22C	109.5
H22A-C22-H22B	109.5	H22A-C22-H22C	109.5
H22B-C22-H22C	109.5	C24-C23-C20	119.46(12)
C28-C23-C20	122.76(13)	C28-C23-C24	117.48(13)
C23-C24-N1	118.83(12)	C25-C24-N1	120.84(13)

C25-C24-C23	120.32(13)	C24-C25-H25	119.9
C26-C25-C24	120.29(14)	C26-C25-H25	119.9
C25-C26-H26	120.0	C27-C26-C25	120.00(15)
C27-C26-H26	120.0	C26-C27-H27	120.3
C26-C27-C28	119.42(14)	C28-C27-H27	120.3
C23-C28-H28	118.8	C27-C28-C23	122.40(14)
C27-C28-H28	118.8	C20-C21-H21A	109.5
C20-C21-H21B	109.5	C20-C21-H21C	109.5
H21A-C21-H21B	109.5	H21A-C21-H21C	109.5
H21B-C21-H21C	109.5	C29-C30-H30	120.1
C31-C30-C29	119.76(15)	C31-C30-H30	120.1
C32-C31-H31	120.0	C30-C31-C32	120.03(16)
C30-C31-H31	120.0		

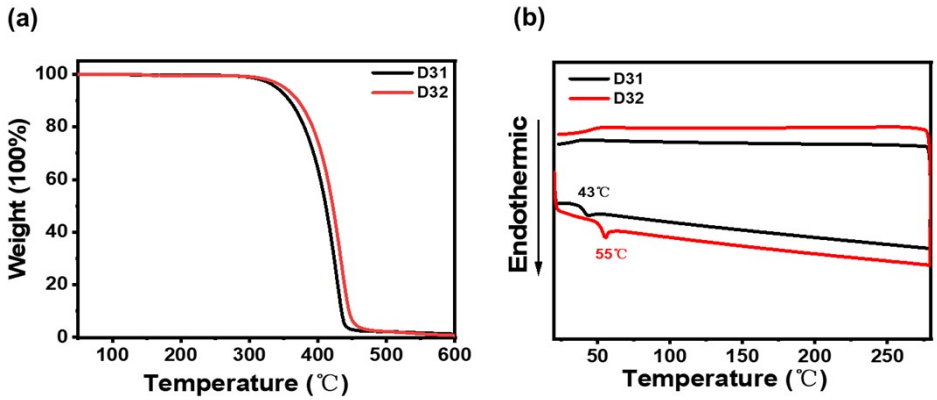

Fig. S8. TGA and DSC curves of D31 and D32.

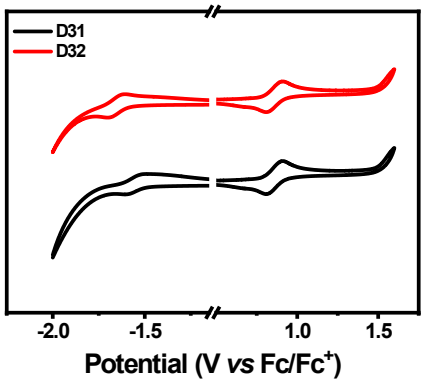

Fig. S9. CV curves of D31 and D32.

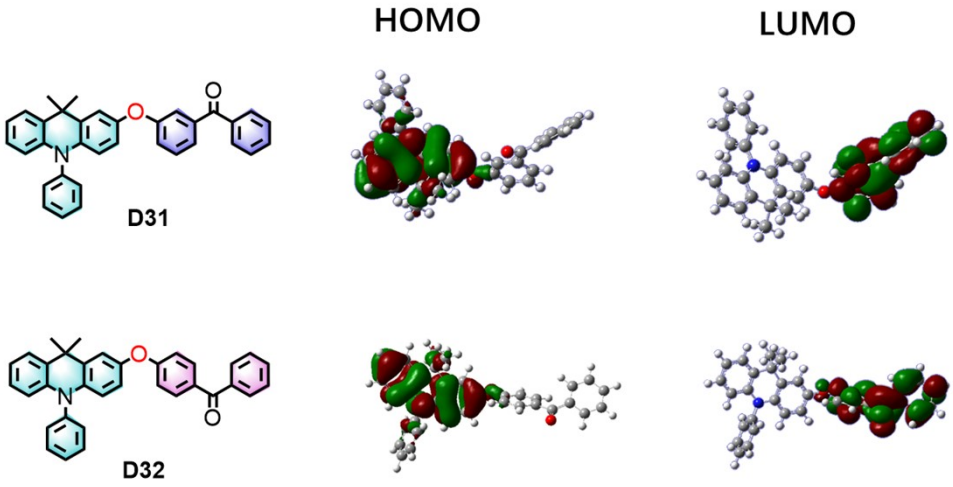

Fig. S10. Calculated HOMO and LUMO distributions of D31and D32.

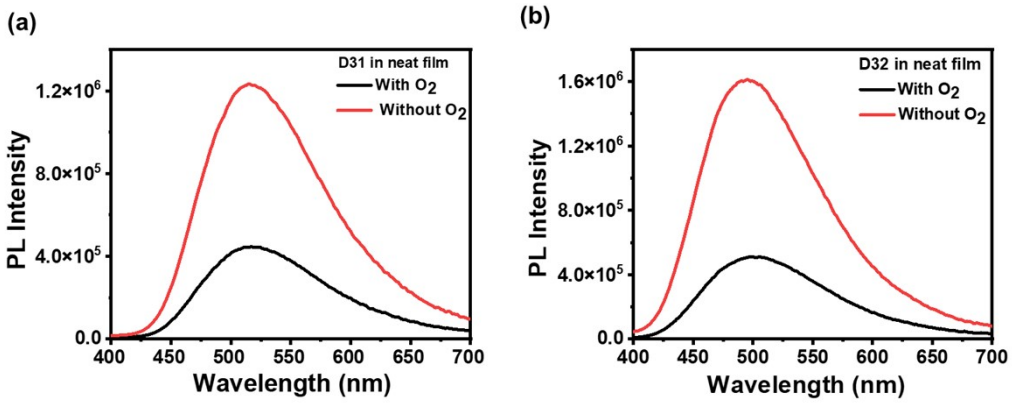

Fig. S11. The O_2 dependence of the PL spectra in neat film for D31 (a) and D32 (b).

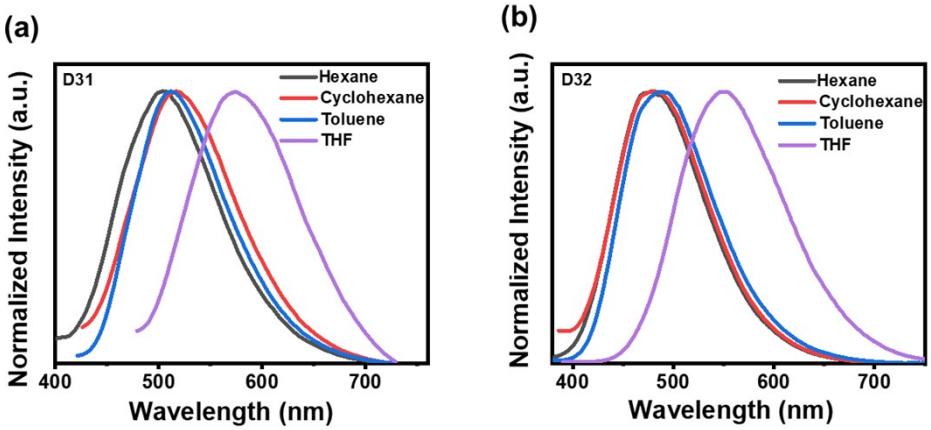

Fig. S12. PL spectra measured in different organic solvents in the presence of O_2 for D31 (a) and D32 (b).

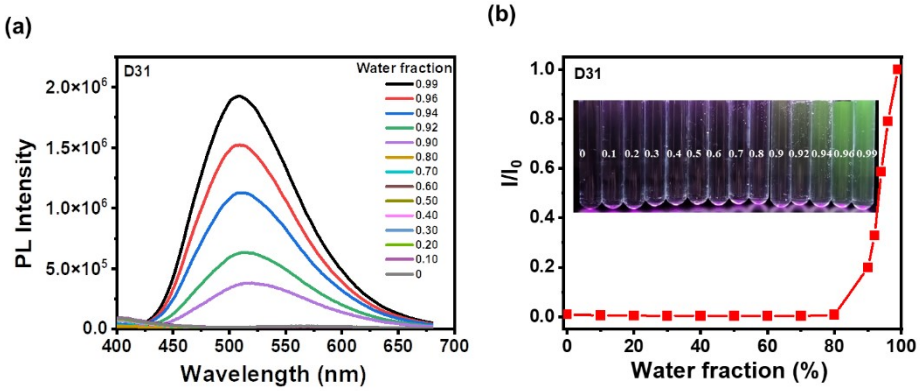

Fig. S13. AIE behavior of D31 in water/THF mixed solvents: (a) Dependence of the PL spectra excited at 350 nm on the water fraction; (b) Relative emission intensity as a function of water fraction, in which I and I_0 represent the PL intensity in water/THF mixed solvents and pure THF solution, respectively. Insets: PL images under UV light with the increasing water fraction from left to right.

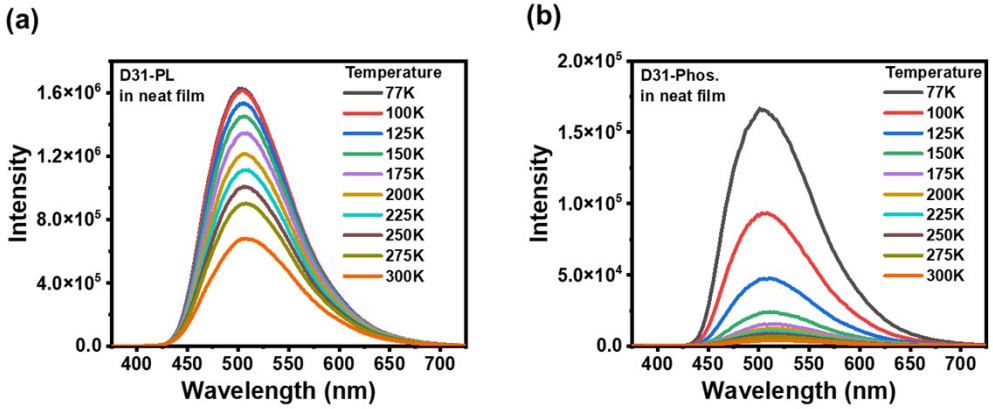

Fig. S14. (a) Temperature-dependent PL spectra (without a delay) for D31 film; (b) Temperature-dependent phosphorescence spectra (with a 0.1 ms delay) for D31 film.

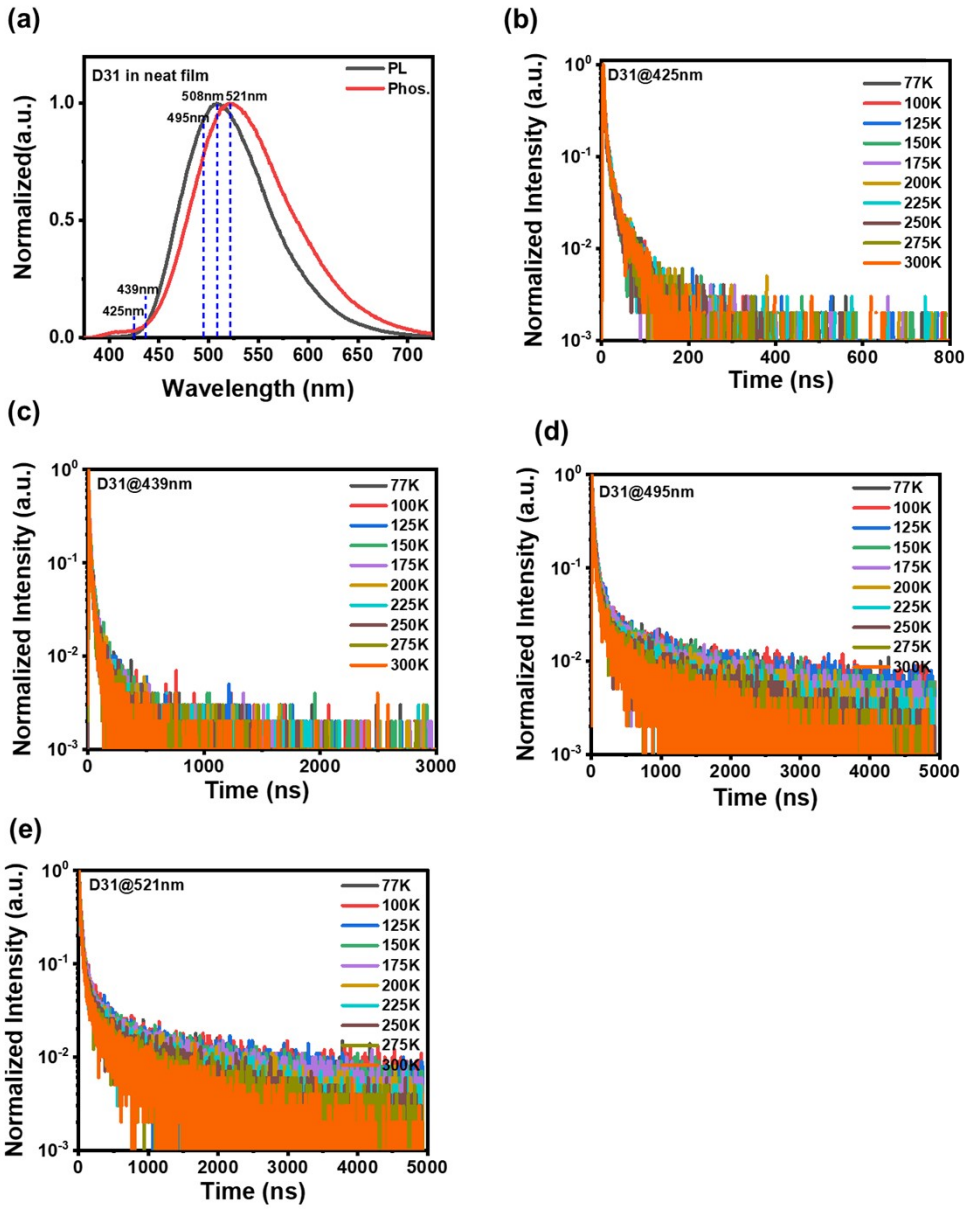

Fig. S15. PL and RTP spectrum (a), Time-dependent transient PL spectra detected at a wavelength of 425 nm (b), 439 nm (c), 495 nm (d) and 521 nm (e) for D31 in neat film.

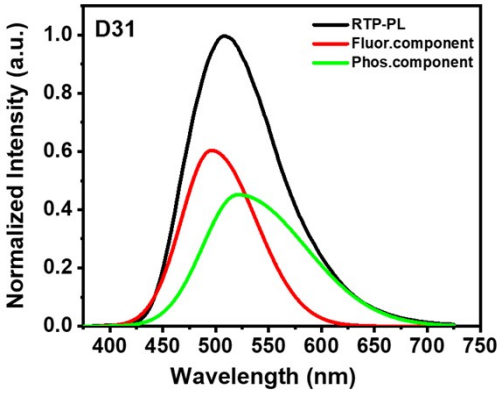

模型	Bigaussian	
方程	if (x < xc) y = y0 + H*exp(-(x - xc)^2/(2*w1^2)); else y = y0 + H*exp(-(x - xc)^2/(2*w2^2));	
绘图	Peak1(Book1_B)	Peak2(Book1_B)
y0	-4.72817E-4 ± 0.0012	-4.72817E-4 ± 0.0012
xc	496 ± 0	521 ± 0
H	0.60431 ± 0.02749	0.45188 ± 0.02737
w1	28.53178 ± 0.32847	33.37608 ± 1.24404
w2	41.97096 ± 1.19814	63.64725 ± 1.25849
Reduced Chi-Sqr	9.29915E-5	
R平方(COD)	0.99922	
调整后R平方	0.99921	

Fig. S16. Bigaussian fitting of the steady-state PL spectra for D31 film. Given that fluorescence is dominated in the TRES spectra at the begging, the peak of TRES spectrum at 1 ns (496 nm) is set as the maximum fluorescent emission. Combined with the maximum phosphorescent emission (521 nm) shown in the RTP spectrum, a Bigaussian fitting is performed to divide the fluorescence and RTP. By comparing their corresponding integral area, the populations of fluorescence and RTP are calculated to be 49.3% and 50.7%, respectively.

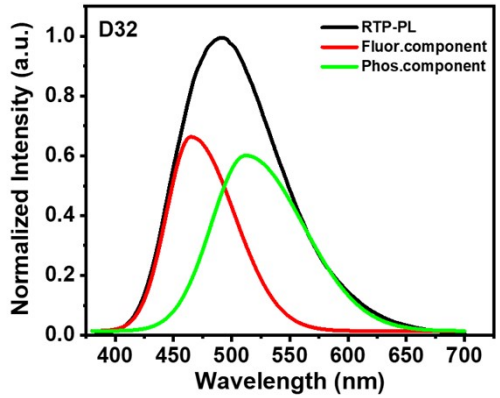

模型	Bigaussian	
方程	if (x < xc) y = y0 + H*exp(-(x - xc)^2/(2*w1^2)); else y = y0 + H*exp(-(x - xc)^2/(2*w2^2));	
绘图	Peak1(Book1_B)	Peak2(Book1_B)
y0	0.01406 ± 0.00137	0.01406 ± 0.00137
xc	465 ± 0	512 ± 0
H	0.6494 ± 0.01291	0.58683 ± 0.01742
w1	21.03023 ± 0.1361	29.68255 ± 1.09412
w2	37.03184 ± 1.56799	49.29449 ± 0.58296
Reduced Chi-Sqr	1.46975E-4	
R平方(COD)	0.99881	
调整后R平方	0.99879	

Fig. S17. Bigaussian fitting of the steady-state PL spectra for D32 film. Given that fluorescence is dominated in the TRES spectra at the begging, the peak of TRES spectrum at 1 ns (465 nm) is set as the maximum fluorescent emission. Combined with the maximum phosphorescent emission (512 nm) shown in the RTP spectrum, a Bigaussian fitting is performed to divide the fluorescence and RTP. By comparing their corresponding integral area, the populations of fluorescence and RTP are calculated to be 43% and 57%, respectively.

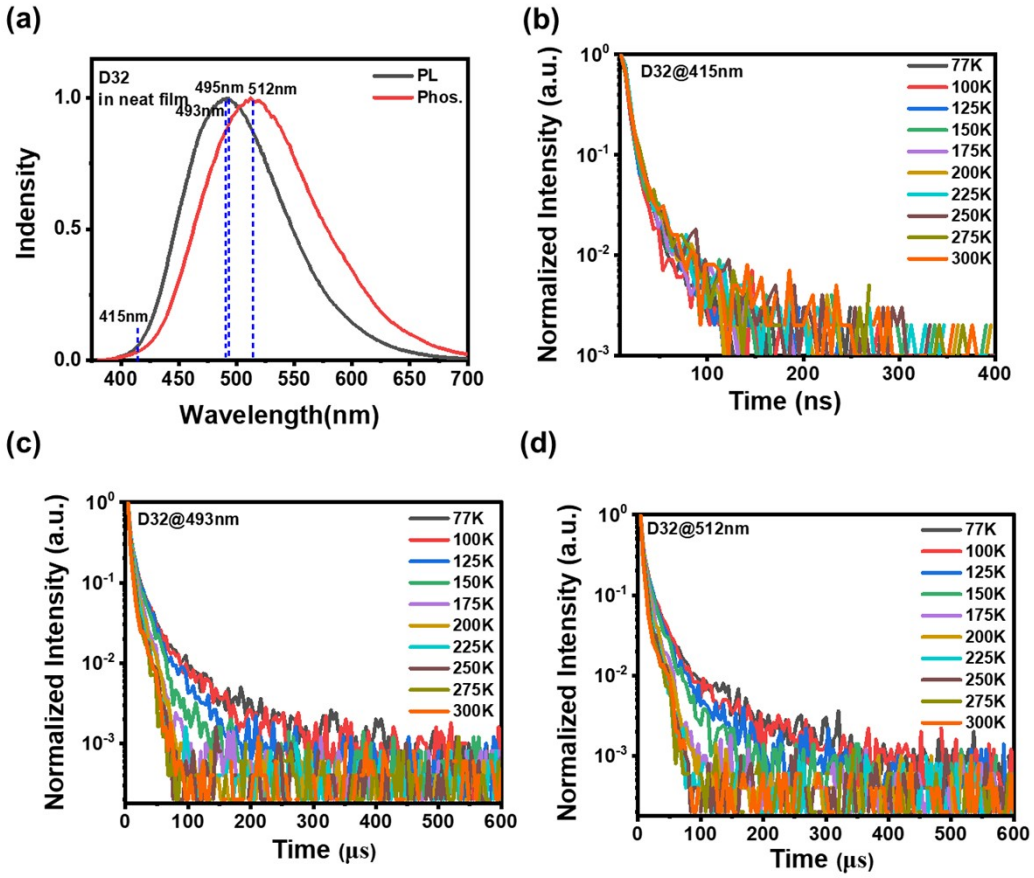

Fig. S18. PL and RTP spectrum (a), Time-dependent transient PL spectra detected at a wavelength of 415 nm (a), 493 nm (b), and 512 nm (c) for D32 in neat film.

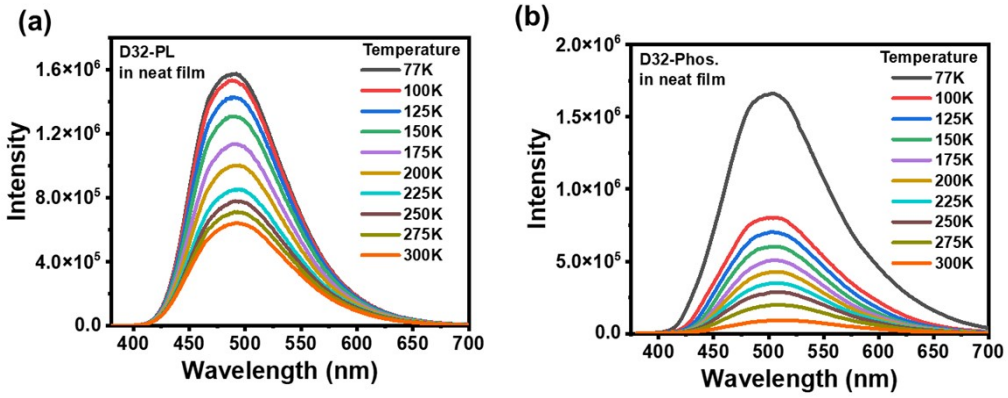

Fig. S19. (a) Temperature-dependent PL spectra (without a delay) for D32 film; (b) Temperature-dependent phosphorescence spectra (with a 0.1 ms delay) for D32 film.

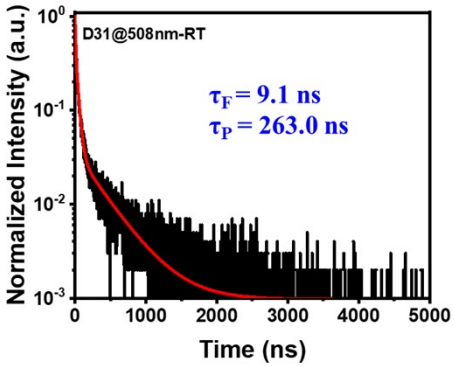

Model	ExpDecay3
Equation	y = y0 + A1*exp(-(x-x0)/t1) + A2*exp(-(x-x0)/t2) + A3*exp(-(x-x0)/t3)
Plot	Normalized1
y0	9.68636E-4 ± 5.206E-5
x0	-1.04845E-11 ± 0
A1	0.51718 ± 0.00713
t1	9.06047 ± 0.14071
A2	0.43947 ± 0.00718
t2	35.97039 ± 0.46019
A3	0.03532 ± 7.49065E-4
t3	387.48878 ± 8.23324
Reduced Chi-Sqr	7.10772E-6
R-Square (COD)	1
Adj. R-Square	1

Fig. S20. Transient PL spectra in neat films for D31 at RT.

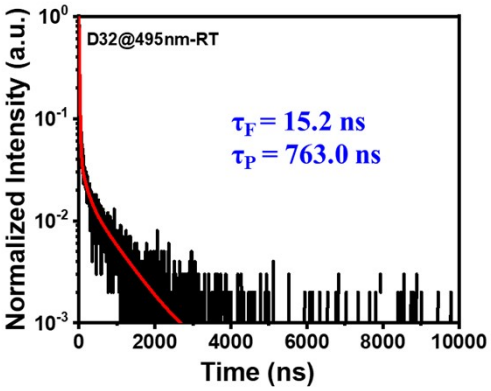

Model	ExpDec3
Equation	y = A1*exp(-x/t1) + A2*exp(-x/t2) + A3*exp(-x/t3) + y0
Plot	Normalized1
y0	4.81579E-4 ± 4.86286E-5
A1	0.36834 ± --
t1	15.67428 ± 36329.49331
A2	0.6709 ± --
t2	15.67437 ± 19945.72176
A3	0.03656 ± 9.44305E-4
t3	439.60122 ± 13.36533
Reduced Chi-Sqr	8.70804E-6
R-Square (COD)	0.98686
Adj. R-Square	0.98685

Fig. S21. Transient PL spectra in neat films for D32 at RT.

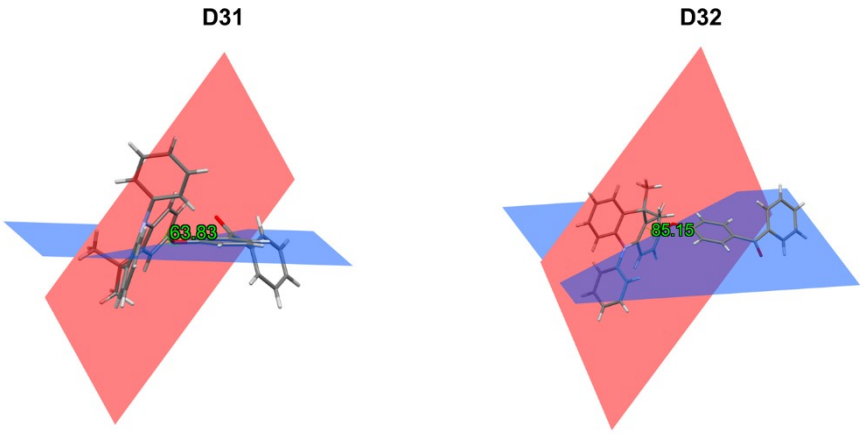

Fig. S22. Dihedral angle between the donor and the acceptor for D31 and D32.

Table S6. Photophysical properties and related parameters of D31 and D32.

Emitter	D31	D32
τ_F (ns)	9.1	15.2

F polulation (%)	49.3	43.0
τ_P (ns)	263.0	763.0
RTP polulation (%)[a]	50.7	57.0
$\Phi_{F(\%)}$ [b]	8.5	12.5
$\Phi_{P(\%)}$ [b]	8.8	16.7
$\Phi_{PL(\%)}$ [b]	17.3	29.2
k_r^F (10^7 S^{-1})[c]	0.93	0.82
k_{nr}^F (10^7 S^{-1})[c]	9.09	4.66
k_r^P (10^6 S^{-1})[c]	0.33	0.22
k_{nr}^P (10^7 S^{-1})[c]	0.35	0.11
k_{ISC} (10^7 S^{-1})[c]	0.97	1.10

[a]Fluorescence (F) and room-temperature phosphorescence (RTP) populations were estimated from Bigaussian fitting of the PL spectra; [b]The PLQYs of fluorescence (Φ_F) and RTP (Φ_P) were determined by the total PLQY (Φ_{PL}) and their corresponding populations; [c]The fluorescence radiative rate (k_r^F), fluorescence non-radiative rate (k_{nr}^F), phosphorescence radiative rate (k_r^P), phosphorescence non-radiative rate (k_{nr}^P) and intersystem crossing rate (k_{ISC}) were obtained by the following equations: $k_r^F = \Phi_F/\tau_F$ $k_{nr}^F = (1-\Phi_F-\Phi_P)/\tau_F$ $k_r^P = \Phi_P/\tau_P$ $k_{nr}^P = (1-\Phi_P)/\tau_P$ $k_{ISC} = \Phi_P/\tau_F$

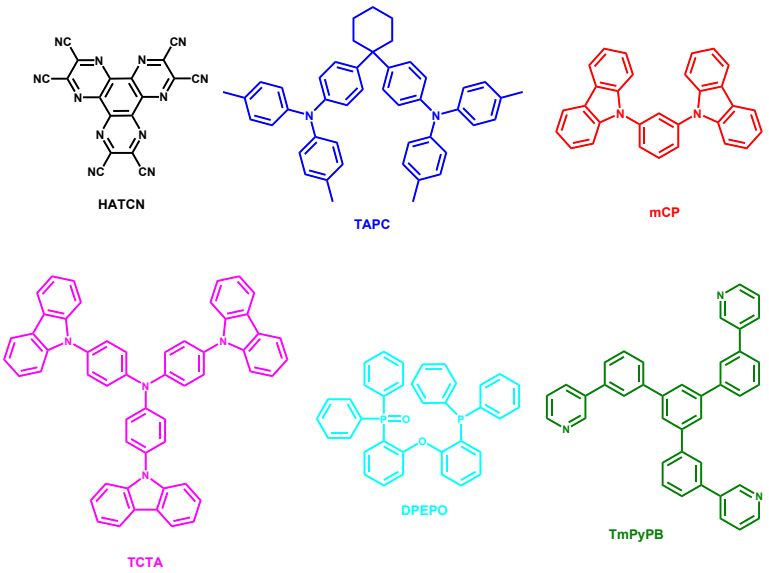

Fig. S23. The materials used in the device.

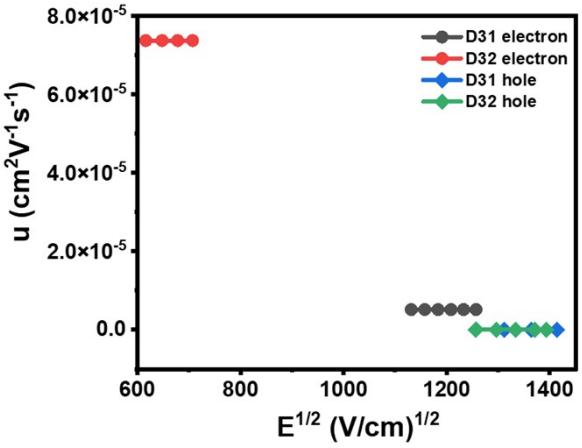

Fig. S24. The carrier transport properties of D31 and D32, in which the electron only device structure is ITO/LiF (1 nm)/D31 or D32 (100 nm)/LiF(1nm)/Al (100 nm), and the hole only device was fabricated with the structure of ITO/MoO_3(2 nm)/D31 or D32 (100 nm)/MoO_3 (5 nm)/Al (100 nm).

Table S7. Summary of hole and electron mobilities of D31 and D32.

Device Structure		**ε_0(F/m)**	**ε_r**	**L(nm)**	**μ($cm^2V^{-1}s^{-1}$)**
EOD	D31	8.854×10^{-12}	3	100	5.16×10^{-6}
	D32			100	7.37×10^{-5}
HOD	D31			100	1.54×10^{-8}
	D32			100	1.49×10^{-8}

ε_0 and ε_r are the vacuum and relative dielectric permittivity; L is the thickness of the device; μ is the carrier mobility.

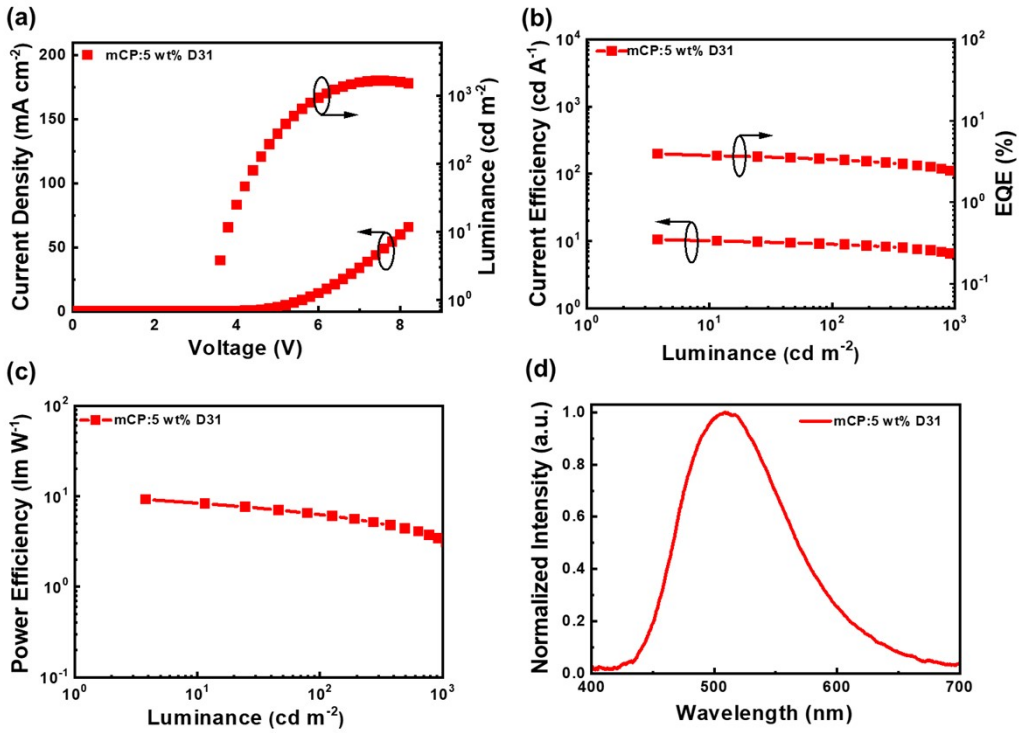

Fig. S25. Doped device performances of 5 wt% D31 in mCP: (a) Current density-luminance-voltage characteristics; (b) Current efficiency-luminance-EQE properties; (c) Power efficiency *versus* luminance curves; (d) EL spectrum.

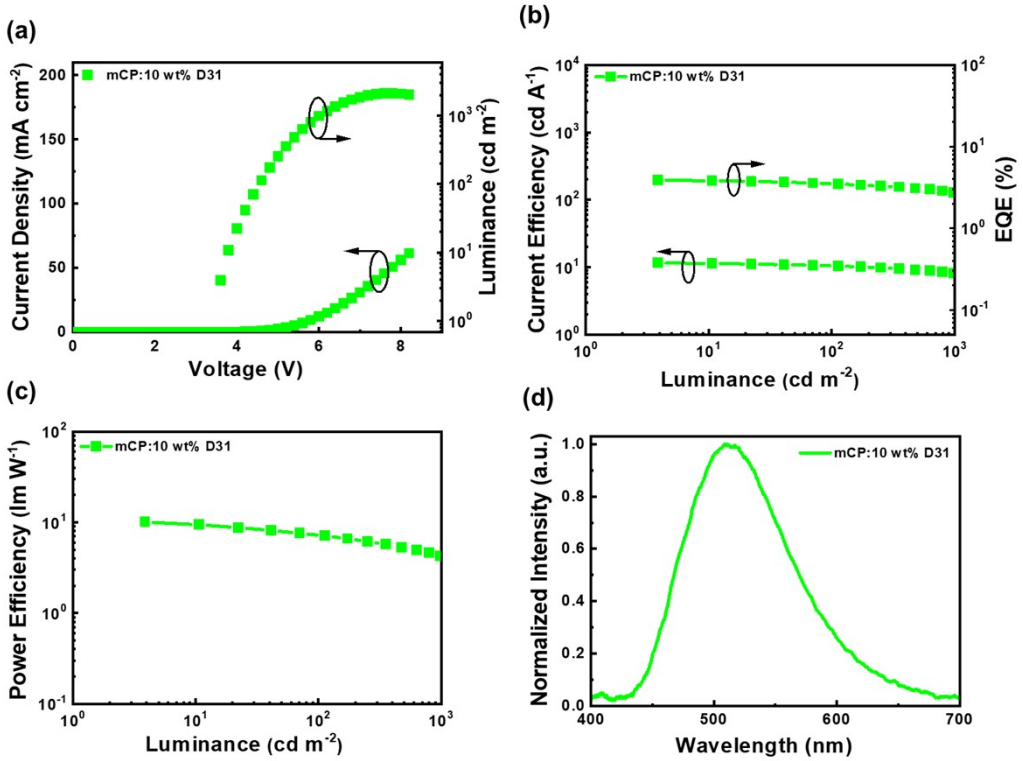

Fig. S26. Doped device performances of 10 wt% D31 in mCP: (a) Current density-luminance-voltage characteristics; (b) Current efficiency-luminance-EQE properties; (c) Power efficiency *versus* luminance curves; (d) EL spectrum.

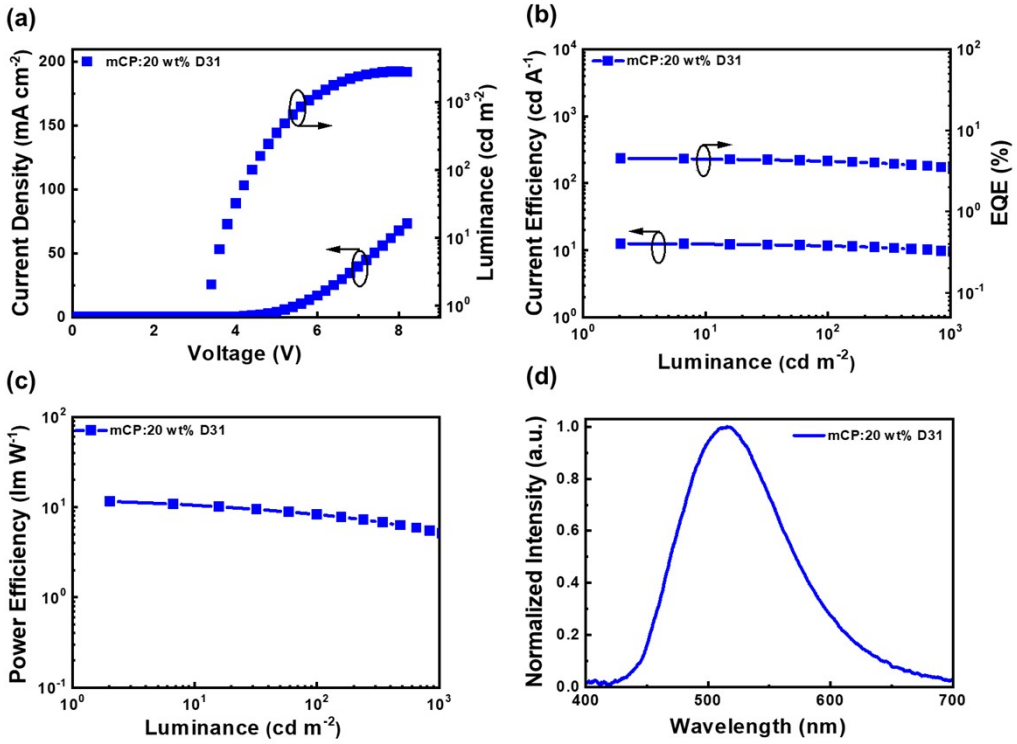

Fig. S27. Doped device performances of 20 wt% D31 in mCP: (a) Current density-luminance-voltage characteristics; (b) Current efficiency-luminance-EQE properties; (c) Power efficiency *versus* luminance curves; (d) EL spectrum.

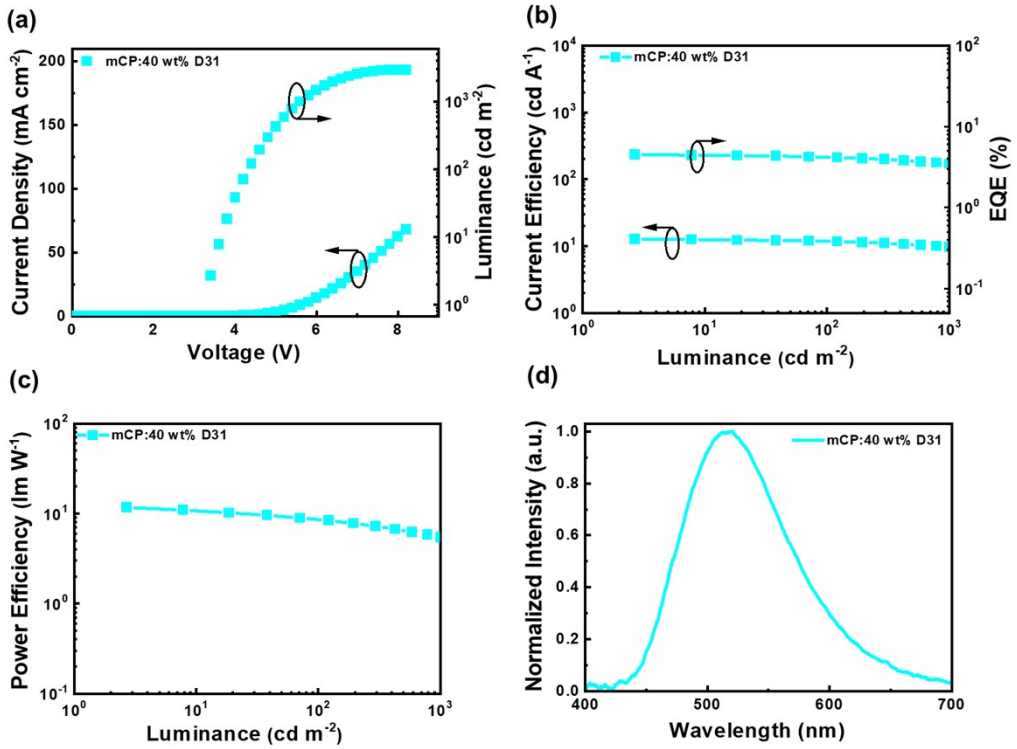

Fig. S28. Doped device performances of 40 wt% D31 in mCP: (a) Current density-luminance-voltage characteristics; (b) Current efficiency-luminance-EQE properties; (c) Power efficiency *versus* luminance curves; (d) EL spectrum.

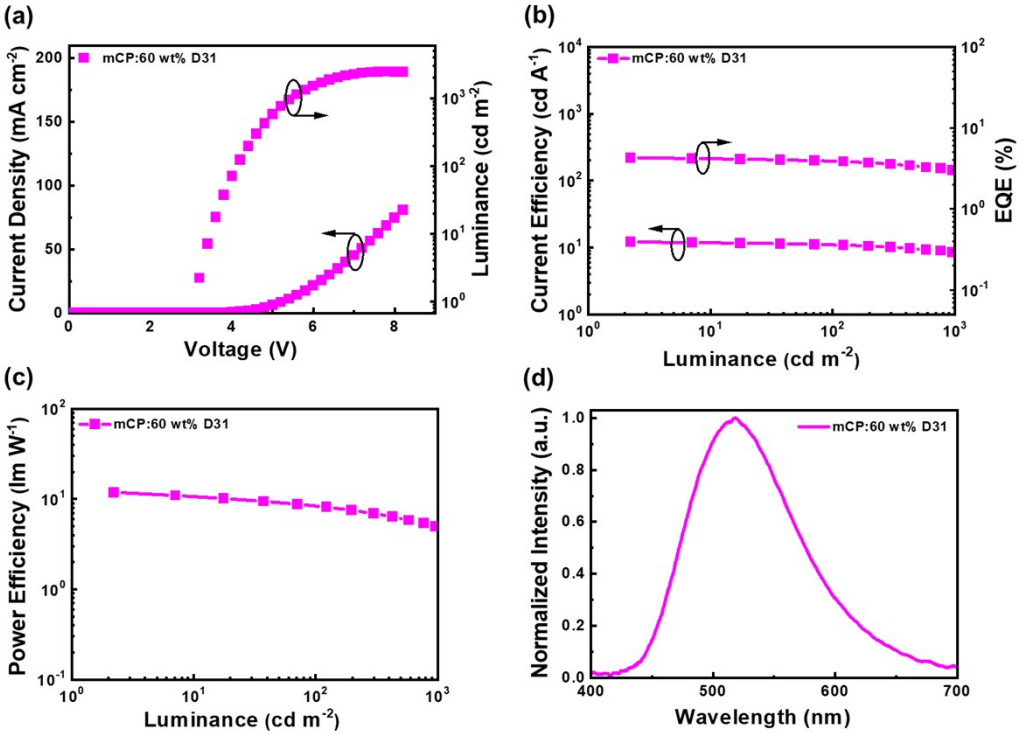

Fig. S29. Doped device performances of 60 wt% D31 in mCP: (a) Current density-luminance-voltage characteristics; (b) Current efficiency-luminance-EQE properties; (c) Power efficiency *versus* luminance curves; (d) EL spectrum.

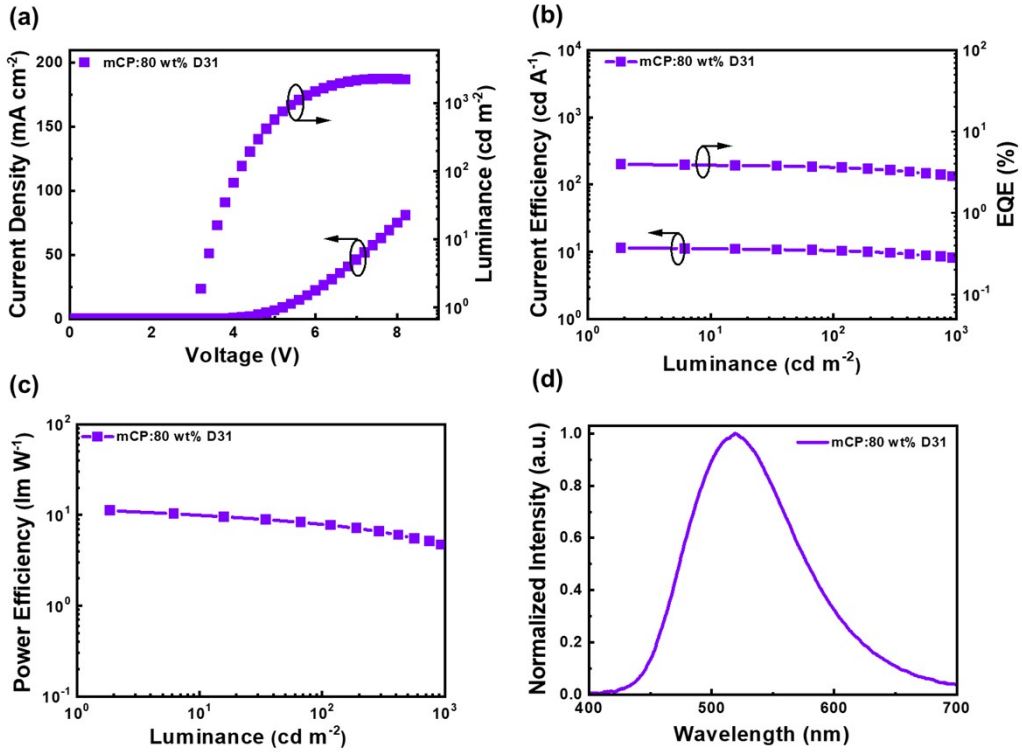

Fig. S30. Doped device performances of 80 wt% D31 in mCP: (a) Current density-luminance-voltage characteristics; (b) Current efficiency-luminance-EQE properties; (c) Power efficiency *versus* luminance curves; (d) EL spectrum.

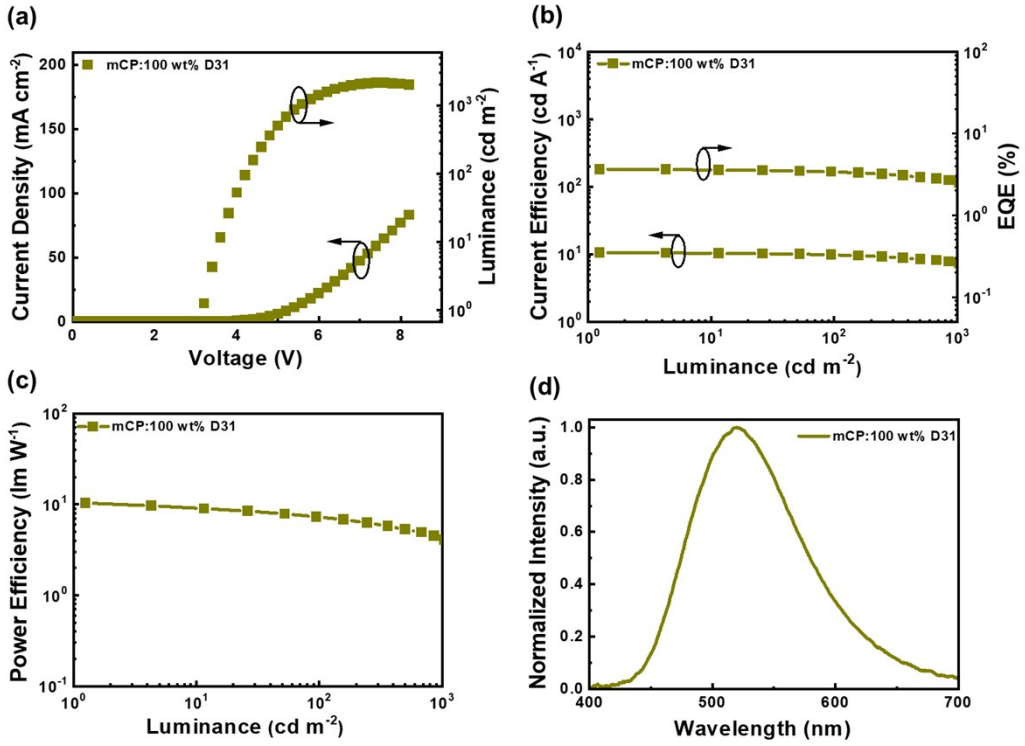

Fig. S31. Non-doped device performances of D31: (a) Current density-luminance-voltage characteristics; (b) Current efficiency-luminance-EQE properties; (c) Power efficiency *versus* luminance curves; (d) EL spectrum.

Table S8. Key EL data of doped and non-doped OLED performances of D31.

EML	V_{on} [a] (V)	L[b] (cd m^{-2})	CE[c] (cd A^{-1})	PE[c] (lm W^{-1})	EQE[c] (%)	CIE[d] (x,y)
mCP:5wt% D31	3.5	1650	10.56/6.15	9.21/3.12	3.94/2.29	0.26,0.47
mCP:10wt% D31	3.5	2106	11.56/7.68	10.09/3.89	3.90/2.60	0.27,0.48
mCP:20wt% D31	3.5	2795	12.51/9.43	11.56/5.11	4.51/3.40	0.27,0.48
mCP:40wt% D31	3.4	2926	12.69/9.69	11.72/5.44	4.51/3.44	0.28,0.49
mCP:60wt% D31	3.2	2468	12.10/8.00	11.88/4.49	4.28/2.83	0.28,0.49
mCP:80wt% D31	3.2	2280	11.37/7.56	11.16/4.24	3.94/2.63	0.29,0.50
D31	3.2	2128	10.55/7.27	10.36/4.08	3.66/2.52	0.29,0.50

[a]Turn-on voltage at 1 cd m^{-2}. [b]Maximum luminance. [c]Data at maximum and 1000 cd m^{-2}. [d]Data at a driving voltage of 6 V.

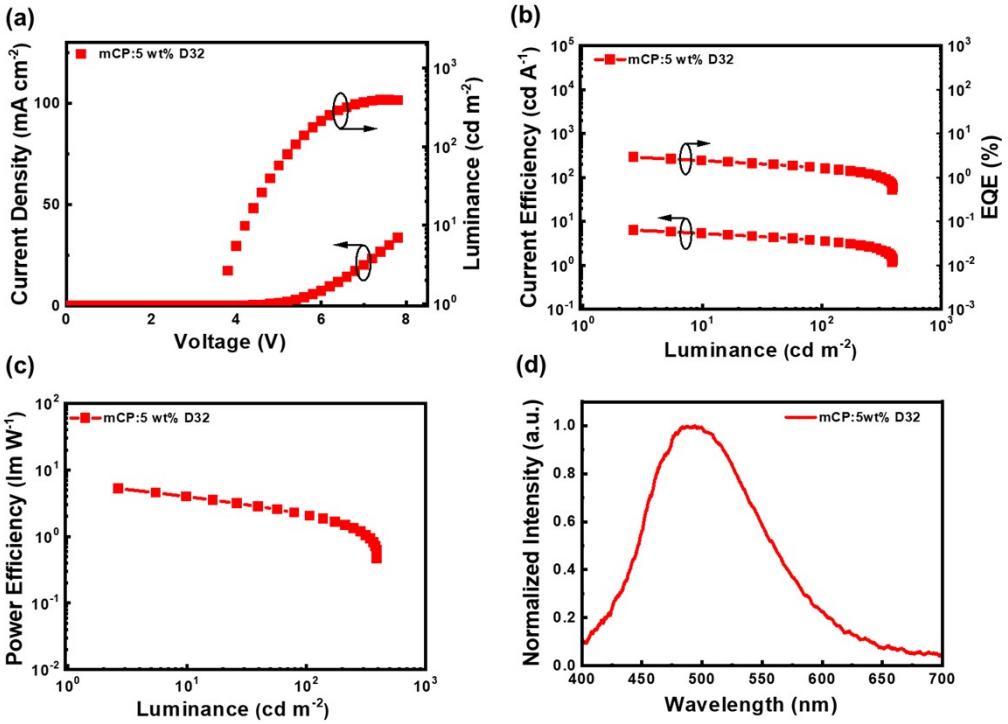

Fig. S32. Doped device performances of 5 wt% D32 in mCP: (a) Current density-luminance-voltage characteristics; (b) Current efficiency-luminance-EQE properties; (c) Power efficiency *versus* luminance curves; (d) EL spectrum.

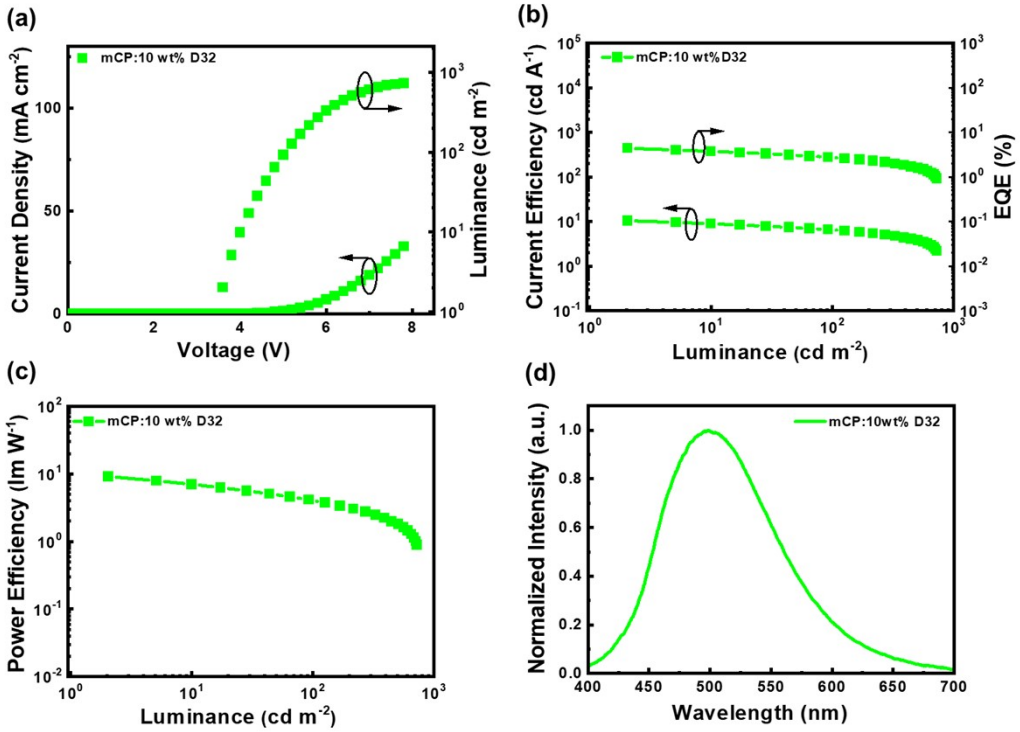

Fig. S33. Doped device performances of 10 wt% D32 in mCP: (a) Current density-luminance-voltage characteristics; (b) Current efficiency-luminance-EQE properties; (c) Power efficiency *versus* luminance curves; (d) EL spectrum.

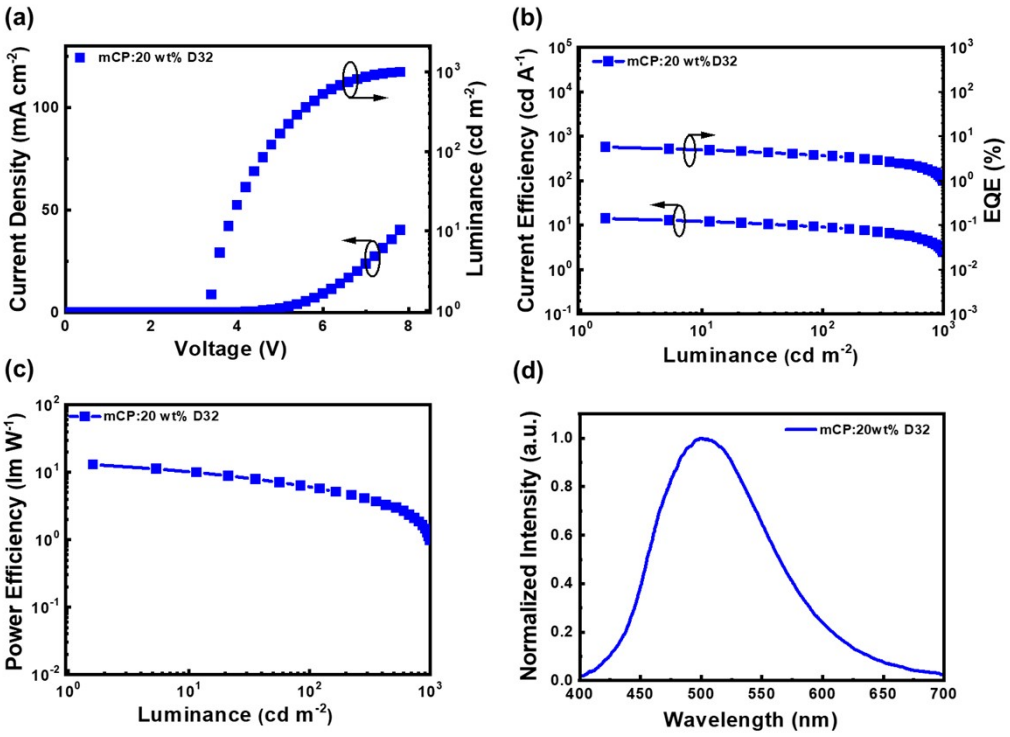

Fig. S34. Doped device performances of 20 wt% D32 in mCP: (a) Current density-luminance-voltage characteristics; (b) Current efficiency-luminance-EQE properties; (c) Power efficiency *versus* luminance curves; (d) EL spectrum.

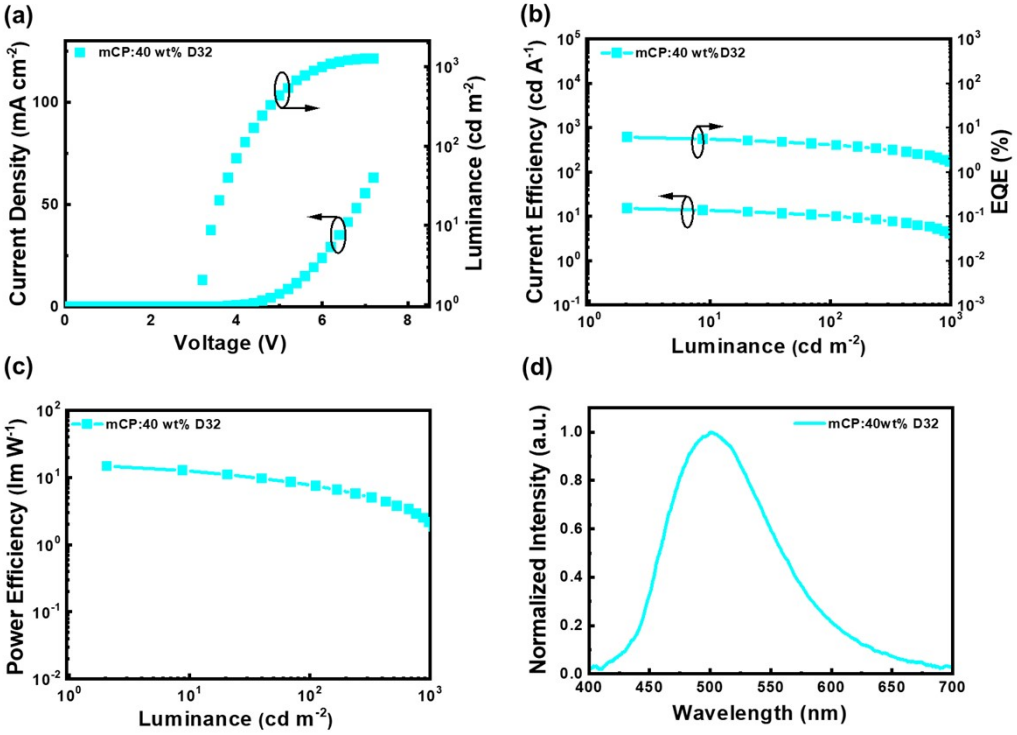

Fig. S35. Doped device performances of 40 wt% D32 in mCP: (a) Current density-luminance-voltage characteristics; (b) Current efficiency-luminance-EQE properties; (c) Power efficiency *versus* luminance curves; (d) EL spectrum.

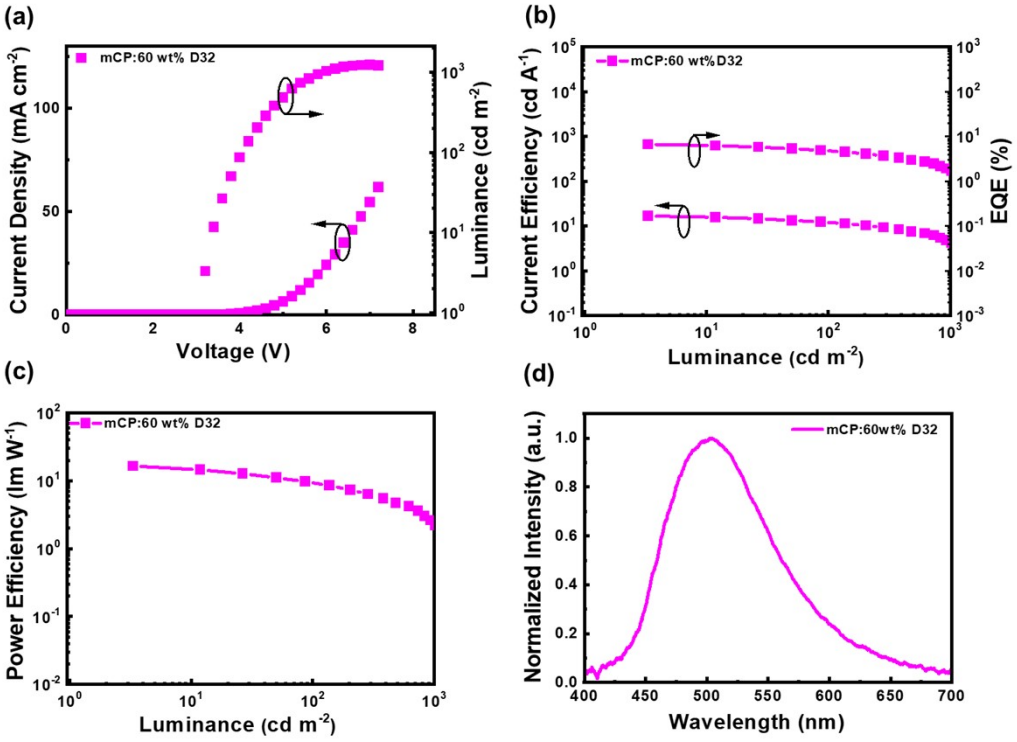

Fig. S36. Doped device performances of 60 wt% D32 in mCP: (a) Current density-luminance-voltage characteristics; (b) Current efficiency-luminance-EQE properties; (c) Power efficiency *versus* luminance curves; (d) EL spectrum.

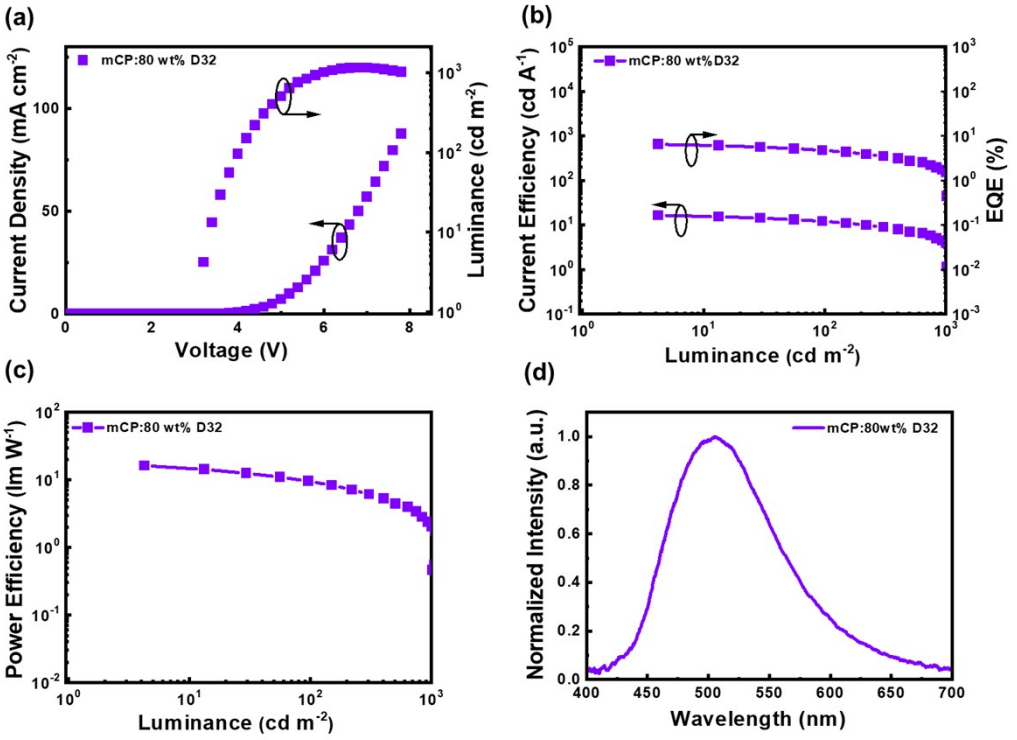

Fig. S37. Doped device performances of 80 wt% D32 in mCP: (a) Current density-luminance-voltage characteristics; (b) Current efficiency-luminance-EQE properties; (c) Power efficiency *versus* luminance curves; (d) EL spectrum.

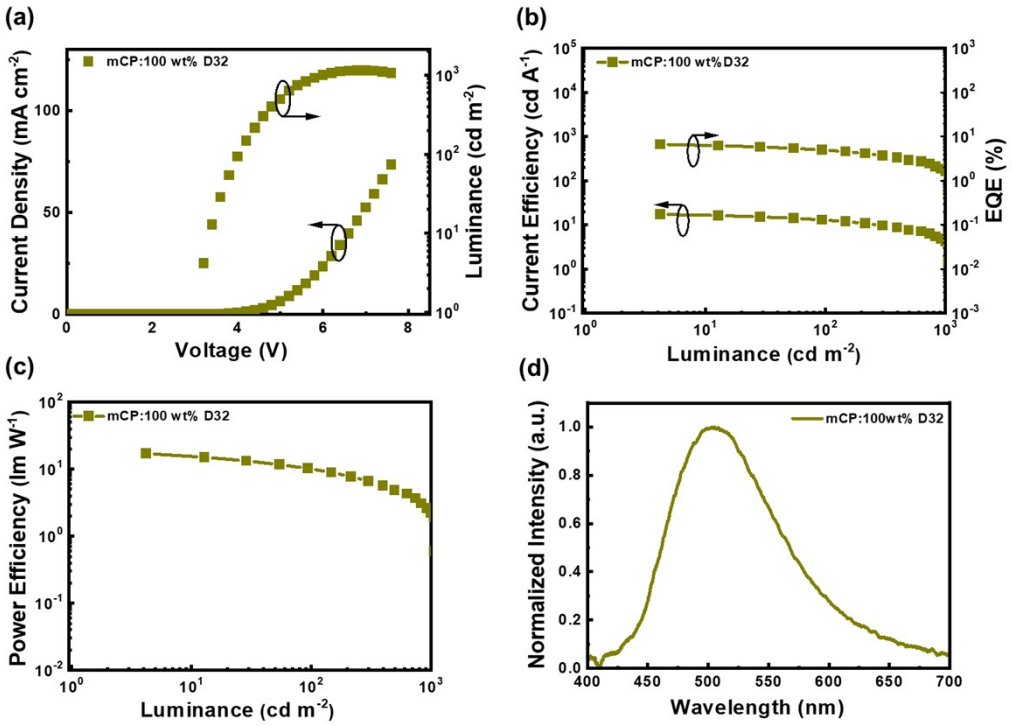

Fig. S38. Non-doped device performances of D32: (a) Current density-luminance-voltage characteristics; (b) Current efficiency-luminance-EQE properties; (c) Power efficiency *versus* luminance curves; (d) EL spectrum.

Table S9. Key EL data of doped and non-doped OLED performances of D32.

EML	V_{on} [a] (V)	L[b] (cd m^{-2})	CE[c] (cd A^{-1})	PE[c] (lm W^{-1})	EQE[c] (%)	CIE[d] (x,y)
mCP:5wt% D32	3.8	392	6.37/-	5.27/-	2.91/-	0.22,0.36
mCP:10wt% D32	3.6	728	10.52/-	9.18/-	4.44/-	0.23,0.39
mCP:20wt% D32	3.4	993	14.10/-	13.03/-	5.73/-	0.24,0.41
mCP:40wt% D32	3.2	1247	15.07/3.67	14.80/1.86	6.10/1.49	0.24,0.42
mCP:60wt% D32	3.2	1221	16.84/4.25	16.54/2.23	6.70/1.69	0.24,0.43
mCP:80wt% D32	3.2	1151	16.52/3.91	16.22/2.05	6.50/1.52	0.24,0.44
D32	3.2	1144	17.39/4.25	17.07/2.23	6.69/1.64	0.25,0.44

[a]Turn-on voltage at 1 cd m^{-2}. [b]Maximum luminance. [c]Data at maximum and 1000 cd m^{-2}. [d]Data at a driving voltage of 6 V.

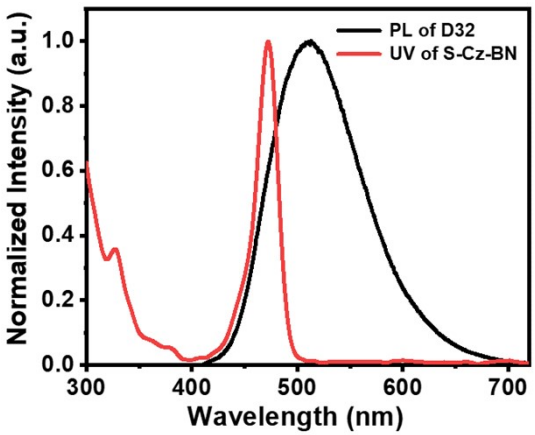

Fig. S39. Overlap between the absorption of S-Cz--BN and the PL of D32.

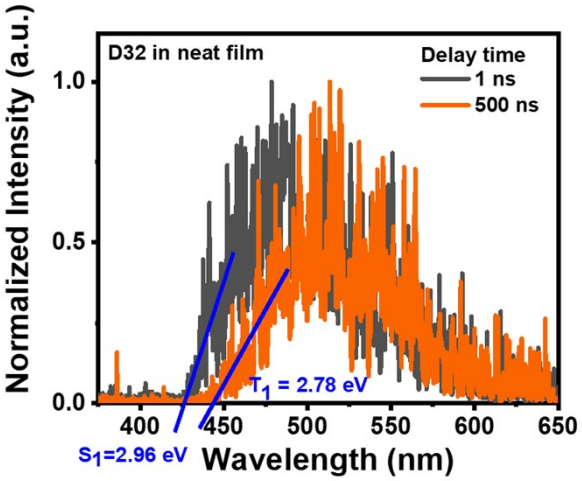

Fig. S40. Determination of the energy levels of S_1 and T_1 for D32. Based on the TRES analysis, it is observed that fluorescence and phosphorescence are the predominant processes in the PL emission at delay times of 1 ns and 500 ns, respectively. Therefore, their onset values can be reasonably considered as the S_1 and T_1 energies of D32. As a result, the energy levels of S_1 and T_1 for D32 are calculated to be 2.96 and 2.78 eV, respectively, using the equation $E = 1240/\lambda_{onset}$, where their onset values are determined to be 419 and 446 nm, respectively.

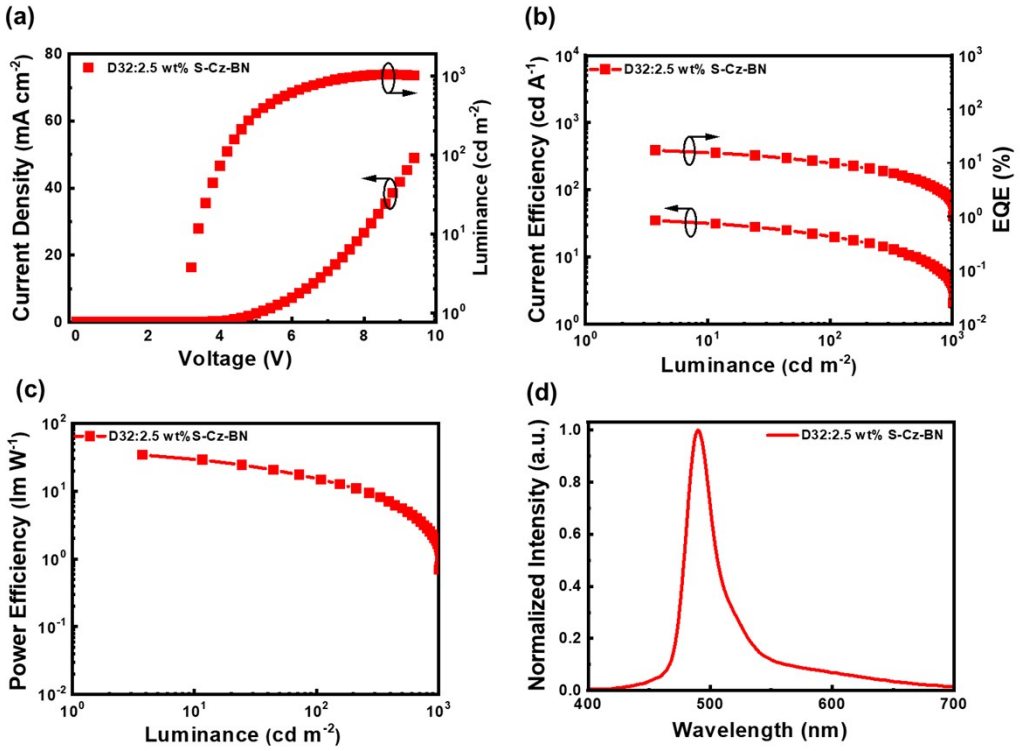

Fig. S41. The sensitization device of D32:2.5 wt% S-Cz-BN: (a) Current density-luminance-voltage characteristics; (b) Current efficiency-luminance-EQE properties; (c) Power efficiency *versus* luminance curves; (d) EL spectrum.

5. Reference

[1] L. Xu, Y. Mo, N. Su, C. Shi, N. Sun, Y. Zhang, L. Duan, Z. -H. Lu, J. Ding. D-O-A based organic phosphors for both aggregation-induced electrophosphorescence and host-free sensitization, *Nat. Commun.* 2023, 14, 1678.